Eur. Phys. J. D **10**, 433–448 (2000)

THE EUROPEAN PHYSICAL JOURNAL D

EDP Sciences

Quantum images in non degenerate optical parametric oscillators

C. Szwaj[1,a], G.-L. Oppo[1,b], A. Gatti[2], and L.A. Lugiato[2]

[1] Department of Physics and Applied Physics, University of Strathclyde, 107 Rottenrow, Glasgow G4 0NG, Scotland, UK
[2] Istituto Nazionale per la Fisica della Materia, Dipartimento di Fisica, Università di Milano, Via Celoria 16, 20133 Milano, Italy

Received 8 October 1999

Abstract. Quantum images, that is inhomogeneous field distributions purely generated by quantum fluctuations, persist when passing from the degenerate to the non-degenerate case of optical parametric oscillators (OPO). Below the threshold for parametric oscillation where the near-field distributions are homogeneous both in intensity and phase, appropriate spatial correlation functions anticipate the transverse spatial pattern that appears above threshold. In particular, the angular dependence of the far field spatial correlation function is able to reveal the travelling-wave nature of the phase pattern above threshold typical of non-degenerate OPOs. Cross-correlation functions between signal and idler intensities show clear evidence of the non-classical nature of the output light.

PACS. 42.50.Dv Nonclassical field states; squeezed, antibunched, and sub-Poissonian states; operational definitions of the phase of the field; phase measurements – 42.65.Sf Dynamics of nonlinear optical systems; optical instabilities, optical chaos and complexity, and optical spatio-temporal dynamics – 42.65.Yj Optical parametric oscillators and amplifiers

1 Introduction

Pattern formation has been widely studied for almost two decades [1], one of the main motivations being that they can be found in as various disciplines as hydrodynamics [1,2], chemistry [3,4], biology [5] and optics [6,7]. The case of optics is, however, peculiar in that optical systems may exhibit quantum effects at room temperature [8] coupled with pattern formation. Recently, the combined effects of quantum fluctuations and spatial structures have been investigated into a general framework [9–14].

The Optical Parametric Oscillator (OPO) is the optimal candidate for the analysis of quantum fluctuations in a pattern forming optical device. From a quantum point of view, the OPO is known to generate non-classical states of light such as squeezed light for a Degenerate OPO (DOPO) [15] or entangled states for a Non Degenerate OPO (NDOPO). From a semiclassical point of view, the interactions between diffraction and nonlinearities results in the generation of spatially modulated output intensities in DOPOs [16] and in phase modulations in NDOPOs [17].

Patterns appearing at threshold in a DOPO are anticipated below threshold in the correlation functions of the quantum fluctuations but not in the average intensity distribution of the near-field [10,13,14]. This phenomenon provides a link between classical and quantum features of the DOPO and has been called "Quantum Image" since information coded in the correlation function does not appear in the mean intensity. Quantum images in a DOPO also display features of non-classical light such as squeezing below the shot noise [10,13,14] and Einstein-Podolsky-Rosen paradoxes [18,19].

In this paper we show that quantum images can also be found in NDOPOs, where the microscopic process of parametric down-conversion consists of the annihilation of a pump photon of frequency $\omega_{\rm p}$ with creation of a signal and an idler photons of frequencies $\omega_{\rm s} = \mu\omega_{\rm p}$ and $\omega_{\rm i} = \nu\omega_{\rm p}$, respectively, with $\mu \neq \nu$ and $\mu + \nu = 1$. Alternatively, the two down-converted photons may have the same frequency but orthogonal polarisations (like in type II OPOs). We recall that, instead, in a DOPO, a pump photon ($\omega_{\rm p}$) is converted into two twin photons both of frequencies $\omega_{\rm p}/2$ (*i.e.* $\mu = \nu = 1/2$), and with the same polarisation (like in type I OPOs). The difference between the two processes is responsible for the different character of the patterns appearing above threshold: standing waves for a DOPO [16], and travelling waves for a NDOPO [17]. We show here that the difference between the patterns appearing above threshold can be already spotted below threshold thanks to the correlation functions of the quantum fluctuations.

The paper is organised as follows. First, we recall some fundamental results of pattern formation in a

[a] *Permanent address*: Laboratoire de Physique des Lasers, Atomes et Molécules, bâtiment P5, Université des Sciences et Technologies de Lille, 59655 Villeneuve d'Ascq, France.
[b] e-mail: gianluca@phys.strath.ac.uk

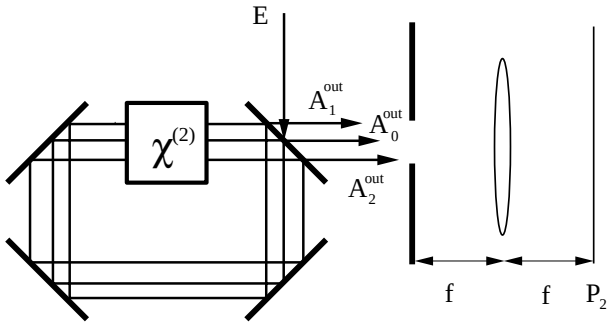

Fig. 1. Configuration of the triply resonant OPO: a ring cavity with a $\chi^{(2)}$ medium inside is pumped with a plane wave E of frequency $\omega_{\rm p}$. The nonlinear crystal generates an output signal field of frequency $\omega_{\rm s}$ and an idler field of frequency $\omega_{\rm i}$. At the output, the aperture of area Q (and width $d_{\rm A}$) and the lens of focal distance f form the far field on the plane P_2.

NDOPO above threshold in Section 2. Then we introduce linear and nonlinear Langevin equations for a triply resonant NDOPO (Sect. 3). We then use the linearised Langevin equations for the signal and idler fluctuations below threshold to calculate explicitly the mean field intensities. In the near-field the intensity distributions are homogeneous in space, both for idler and signal, while in the far-field they are peaked around two rings, that anticipate the off-axis emission above threshold. In Section 4 we show that both the near-field and the far-field correlation functions of signal and idler fields taken separately provide information about the generation of phase waves above threshold. Moreover, we demonstrate that all the non-classical effects are displayed in cross-correlations such as the difference in photo-counts between signal and idler photo-counters. Finally, in Section 5 we study the transition from a NDOPO quantum image below threshold to a NDOPO classical image above threshold by using the nonlinear Langevin equations.

2 Pattern formation in a non degenerate OPO above threshold

We consider first a triply resonant non degenerate OPO. A $\chi^{(2)}$ nonlinear crystal is placed in a ring optical cavity formed by 4 mirrors (see Fig. 1), among which only one is transmitting at the signal and idler frequencies. The system is pumped by a coherent field $\mathcal{E}_{\rm in}$, with a plane-wave configuration and a frequency $\omega_{\rm p}$. The crystal partially down-converts light at the pump frequency $\omega_{\rm p}$ into light at the signal frequency $\omega_{\rm s} = \mu\omega_{\rm p}$ and the idler frequency $\omega_{\rm i} = \nu\omega_{\rm p}$ where μ and ν verify $\mu + \nu = 1$.

We describe the evolution of the system using semiclassical equations for the slowly varying field distributions $\mathcal{A}_0(\mathbf{x}, t)$, $\mathcal{A}_1(\mathbf{x}, t)$ and $\mathcal{A}_2(\mathbf{x}, t)$ associated with the pump, signal and idler waves, respectively. They depend only on time and on the transverse coordinates $\mathbf{x} = (x, y)$, while the dependence of the longitudinal coordinate z has been removed *via* the mean field limit. This means that only the closest longitudinal cavity mode is taken into consideration for the pump, signal and idler waves, respectively. We have the following set of equations [20]:

$$\frac{\partial}{\partial t}\mathcal{A}_0 = \gamma_0[-(1 + {\rm i}\delta_0 - {\rm i}a_0\nabla^2)\mathcal{A}_0 + E - \mathcal{A}_1\mathcal{A}_2] \quad (1a)$$

$$\frac{\partial}{\partial t}\mathcal{A}_1 = \gamma_1[-(1 + {\rm i}\delta_1 - {\rm i}a_1\nabla^2)\mathcal{A}_1 + \mathcal{A}_0\mathcal{A}_2^*] \quad (1b)$$

$$\frac{\partial}{\partial t}\mathcal{A}_2 = \gamma_2[-(1 + {\rm i}\delta_2 - {\rm i}a_2\nabla^2)\mathcal{A}_2 + \mathcal{A}_0\mathcal{A}_1^*], \quad (1c)$$

where γ_0, γ_1, γ_2 are the cavity damping rates for the pump, signal and idler respectively. The detuning are defined as

$$\delta_0 = \frac{\omega_0 - \omega_{\rm p}}{\gamma_0}, \quad \delta_1 = \frac{\omega_1 - \mu\omega_{\rm p}}{\gamma_1}, \quad \delta_2 = \frac{\omega_2 - \nu\omega_{\rm p}}{\gamma_2}$$

for the pump, signal and idler respectively, ω_0, ω_1 and ω_2 are the longitudinal cavity frequencies closest to the pump, signal and idler frequencies. The diffraction is described in the paraxial approximation by the transverse Laplacian

$$\nabla^2 = \frac{\partial^2}{\partial x^2} + \frac{\partial^2}{\partial y^2}.$$

x and y are dimensionless transverse coordinates scaled to

$$l_{\rm d} = \left(\frac{c^2}{2\gamma_1\omega_{\rm p}\mu}\right)^{1/2}, \quad (2)$$

i.e. the characteristic length for patterns formation in the cavity. a_j (for $j = 0, 1, 2$) are the diffraction coefficients defined by

$$a_0 = \frac{\mu\gamma_1}{\gamma_0}, \quad a_1 = 1, \quad a_2 = \frac{\mu\gamma_1}{\nu\gamma_2},$$

E is the scaled amplitude of the input field $\mathcal{E}_{\rm in}$. In the derivation of equations (1), we have normalised the field amplitudes $\mathcal{A}_0$, $\mathcal{A}_1$ and $\mathcal{A}_2$ to $(\gamma_1\gamma_2)^{1/2}/(gL(\mu\nu)^{1/2})$, $(\gamma_0\gamma_2)^{1/2}/(gL\nu^{1/2})$ and $(\gamma_0\gamma_1)^{1/2}/(gL\mu^{1/2})$, respectively, with g being the coupling constant of the interaction among the three fields due to the non linear material of length L.

Equations (1) are invariant under the transformation

$$\tilde{\mathcal{A}}_1 = \mathcal{A}_1{\rm e}^{{\rm i}\omega t} \quad \tilde{\mathcal{A}}_2 = \mathcal{A}_2{\rm e}^{-{\rm i}\omega t} \quad (3)$$

apart from a trivial shift of the detunings

$$\tilde{\delta}_1 = \frac{\omega_1 - \mu\omega_{\rm p} - \omega}{\gamma_1} \quad \tilde{\delta}_2 = \frac{\omega_2 - \nu\omega_{\rm p} + \omega}{\gamma_2}\,. \quad (4)$$

By selecting the frequency reference ω such that homogeneous solutions above threshold are stationary, equations (1) can be rewritten as

$$\frac{\partial}{\partial t}\mathcal{A}_0 = \gamma_0[-(1 + {\rm i}\delta_0 - {\rm i}a_0\nabla^2)\mathcal{A}_0 + E - \mathcal{A}_1\mathcal{A}_2] \quad (5a)$$

$$\frac{\partial}{\partial t}\mathcal{A}_1 = \gamma_1[-(1 + {\rm i}\Delta - {\rm i}a_1\nabla^2)\mathcal{A}_1 + \mathcal{A}_0\mathcal{A}_2^*] \quad (5b)$$

$$\frac{\partial}{\partial t}\mathcal{A}_2 = \gamma_2[-(1 + {\rm i}\Delta - {\rm i}a_2\nabla^2)\mathcal{A}_2 + \mathcal{A}_0\mathcal{A}_1^*], \quad (5c)$$

where we have omitted the tildas of transformation (3) and introduced the equivalent detuning $\Delta = (\gamma_1\delta_1 + \gamma_2\delta_2)/(\gamma_1+\gamma_2)$. This means that the dynamics of many choices of detunings values are described by a single equations if the value of Δ is kept fixed.

Below threshold the stationary states of the pump, signal and idler fields are specified by

$$\mathcal{A}_0 = \frac{E}{1+\mathrm{i}\delta_0}, \quad \mathcal{A}_1 = \mathcal{A}_2 = 0. \tag{6}$$

Equations (5) describe also the situation where signal and idler fields have the same frequency ($\mu = \nu = 1/2$), but orthogonal linear polarisations (type II OPOs). When the input field E increases, a bifurcation occurs corresponding to the loss of stability of the steady state (6) and the generation of a signal and idler field. It has been shown [16,17, 20] that diffraction causes the threshold intensity and the character of the solution above threshold to depend on the sign of the equivalent detuning Δ. For positive value of Δ and $\delta_0 = 0$, the trivial solution (6) become unstable when the pump intensity reaches the threshold value $\sqrt{1+\Delta^2}$ which corresponds to a critical wave number $k_\mathrm{c} = 0$; as a consequence signal and idler fields emitted immediately above threshold are homogeneous in space. For a negative value of Δ and $\delta_0 = 0$, the most unstable mode corresponds to a wave vector of magnitude

$$k_\mathrm{c} = \sqrt{-\Delta(\gamma_1+\gamma_2)/(\gamma_1 a_1 + \gamma_2 a_2)}. \tag{7}$$

The threshold for this transition is $\mathcal{A}_0 = 1$, hence lower than that for positive detuning. Longhi has shown that above threshold a pure Traveling Wave (TW) can appear with a wavenumber k_c [17]. We recall that in the case of the DOPO, the corresponding stable pattern at threshold is a standing wave, *i.e.* the superimposition of two TWs with opposite wavevectors [16]. Two comments are in order. First, any orientation of the traveling wave in the transverse plane is possible, depending only on the initial conditions (noise). Second, the TWs are not the only possible patterns stable at threshold in a NDOPO with $\delta_0 \neq 0$; alternating rolls are also allowed as shown in [17]. Similarly, standing waves are not the only possible patterns stable at threshold in a DOPO with $\delta_0 \neq 0$, where squares, hexagons, quasicrystals can also be found in both mean field [22] and non mean field models [23]. Here, we consider parameter values (mainly $\delta_0 = 0$) corresponding to the simplest case of pure TWs above threshold. Other cases will be considered in future work.

As for the case of the DOPO, we will show that also in NDOPOs the pattern which appears above threshold is anticipated below threshold by the quantum fluctuations. Hence for the NDOPO the quantum images will display the features of the TW structure emerging at onset.

Finally, we point out that all the above considerations are also valid for the doubly resonant NDOPO configuration where the pump field is not resonated. By following a procedure similar to reference [21] where the mean field limit is extended to the DOPO case with non resonated pump, we obtain the following set of equations for a doubly resonant NDOPO:

$$\frac{\partial}{\partial t}\mathcal{A}_1 = \gamma_1[-(1+\mathrm{i}\Delta - \mathrm{i}a_1\nabla^2)\mathcal{A}_1 + E\mathcal{A}_2^* - \mathcal{A}_1|\mathcal{A}_2|^2] \tag{8a}$$

$$\frac{\partial}{\partial t}\mathcal{A}_2 = \gamma_2[-(1+\mathrm{i}\Delta - \mathrm{i}a_2\nabla^2)\mathcal{A}_2 + E\mathcal{A}_1^* - \mathcal{A}_2|\mathcal{A}_1|^2]. \tag{8b}$$

3 Quantum Langevin equations and quantum images below threshold

In order to describe the quantum fluctuations in the system, we derive the Langevin equations for the field distributions $\alpha_0(\mathbf{x},t)$, $\alpha_1(\mathbf{x},t)$ and $\alpha_2(\mathbf{x},t)$ associated with the pump, the signal and the idler respectively. The procedure is a generalisation for a NDOPO of the approach used in the case of the DOPO [14,24]. We consider the master equation for the density operator of the system. Using the Wigner representation, this master equation is transformed into a Fokker-Planck equation for the Wigner functional. The third order functional derivatives are neglected. Then this equation is finally transformed into a set of classical-looking Langevin equations for the scaled field envelopes of the pump, signal and idler, respectively

$$\frac{\partial}{\partial t}\alpha_0 = \gamma_0\Big[-(1+\mathrm{i}\delta_0 - \mathrm{i}a_0\nabla^2)\alpha_0 + E - \alpha_1\alpha_2 + \sqrt{\frac{2}{\gamma_0 n_\mathrm{th}}}\xi_0(\mathbf{x},t)\Big] \tag{9a}$$

$$\frac{\partial}{\partial t}\alpha_1 = \gamma_1\Big[-(1+\mathrm{i}\Delta - \mathrm{i}a_1\nabla^2)\alpha_1 + \alpha_0\alpha_2^* + \sqrt{\frac{2}{\gamma_0 n_\mathrm{th}}}\xi_1(\mathbf{x},t)\Big] \tag{9b}$$

$$\frac{\partial}{\partial t}\alpha_2 = \gamma_2\Big[-(1+\mathrm{i}\Delta - \mathrm{i}a_2\nabla^2)\alpha_2 + \alpha_0\alpha_1^* + \sqrt{\frac{2}{\gamma_0 n_\mathrm{th}}}\xi_2(\mathbf{x},t)\Big]. \tag{9c}$$

The Langevin force terms ξ_l are described by stationary Gaussian stochastic processes with zero average and correlation functions given by:

$$\langle\xi_l^*(\mathbf{x},t)\xi_j(\mathbf{x}',t')\rangle = \frac{1}{2}\delta(\mathbf{x}-\mathbf{x}')\delta(t-t')\delta_{lj} \tag{10a}$$

$$\langle\xi_l(\mathbf{x},t)\xi_j(\mathbf{x}',t')\rangle = 0, \tag{10b}$$

with l and $j = 0,1,2$. The parameter n_th, whose inverse measures the level of quantum noise, is given by

$$n_\mathrm{th} = \frac{\gamma_1\gamma_2}{g^2}l_\mathrm{d}^2. \tag{11}$$

The parameter n_th represents the photon number needed to trig the emission of a signal and an idler field at threshold. Langevin equations analogous to (9) can also be obtained for the doubly resonant NDOPO case.

In order to perform analytical calculations we analyse a linearised version of the model (9). Let

$$\alpha_l(\mathbf{x},t) = \mathcal{A}_l(\mathbf{x},t) + \sqrt{\frac{\gamma_l}{\gamma_0 n_{\rm th}}}\Delta\alpha_l(\mathbf{x},t), \tag{12}$$

with ($l = 0,1,2$), where $\mathcal{A}_l(\mathbf{x},t)$ are the classical fields whose evolution is described by equations (5) or (8) and $\Delta\alpha_l(\mathbf{x},t)$ are stochastic variables representing quantum fluctuations around classical mean fields. As shown in equations (6), the stationary averaged values of the signal and idler field below threshold are zero. Therefore, the pump decouples from the signal and idler in the Langevin equations for $\Delta\alpha_l$. This means that the linearised Langevin equations describe simultaneously both the triply and doubly resonant NDOPO cases. We focus our attention on the dynamics of the signal and idler fluctuations and consider the following equations:

$$\frac{\partial}{\partial t}\Delta\alpha_1 = \gamma_1\left[-(1+\mathrm{i}\Delta-\mathrm{i}a_1\nabla^2)\Delta\alpha_1 + \mathcal{A}_0\sqrt{\frac{\gamma_2}{\gamma_1}}\Delta\alpha_2^*\right] + \sqrt{2\gamma_1}\xi_1(\mathbf{x},t) \tag{13a}$$

$$\frac{\partial}{\partial t}\Delta\alpha_2 = \gamma_2\left[-(1+\mathrm{i}\Delta-\mathrm{i}a_2\nabla^2)\Delta\alpha_2 + \mathcal{A}_0\sqrt{\frac{\gamma_1}{\gamma_2}}\Delta\alpha_1^*\right] + \sqrt{2\gamma_2}\xi_2(\mathbf{x},t). \tag{13b}$$

The coupled equations (13) are linear stochastic partial differential equations which allow analytical solutions for the correlation functions in the Fourier domain. We introduce:

$$\beta_l(\mathbf{k},t) = \frac{1}{2\pi}\int \mathrm{d}^2\mathbf{x}\ \Delta\alpha_l(\mathbf{x},t)\mathrm{e}^{\mathrm{i}\mathbf{k}\cdot\mathbf{x}}, \tag{14}$$

where $l = 1,2$, $\mathbf{k}$ being the transverse wave vector $\mathbf{k} = (k_x,k_y)$.

We note that, with the scaling (12), the stochastic variables $\Delta\alpha_l$ correspond in the Wigner representation to the intracavity field operators obeying for equal times the standard commutation relations

$$\left[A_l(\mathbf{x},t), A_l^\dagger(\mathbf{x}',t)\right] = \delta(\mathbf{x}-\mathbf{x}') \tag{15}$$

(with respect to the scaled spatial variable $\mathbf{x}$). Let us remind that the Wigner representation provides the expectation values of symmetrically ordered products of field operators. For example

$$\langle\Delta\alpha_l^*(\mathbf{x})\Delta\alpha_l(\mathbf{x}')\rangle = \frac{1}{2}[\langle A_l^\dagger(\mathbf{x})A_l(\mathbf{x}')\rangle + \langle A_l(\mathbf{x})A_l^\dagger(\mathbf{x}')\rangle] = \langle A_l^\dagger(\mathbf{x})A_l(\mathbf{x}')\rangle + \frac{1}{2}\delta(\mathbf{x}-\mathbf{x}'), \tag{16}$$

while in the Fourier plane

$$\langle\beta_l^*(\mathbf{k})\beta_l(\mathbf{k}')\rangle = \langle A_l^\dagger(\mathbf{k})A_l(\mathbf{k}')\rangle + \frac{1}{2}\delta(\mathbf{k}-\mathbf{k}'). \tag{17}$$

Note that in equations (16, 17) we have omitted the temporal dependence of the variables in the correlation functions. Whenever the time dependence does not appear explicitly in the following, we assume equal time correlations.

We recall that by using the standard input-output cavity formalism [25] the normally ordered expectation values outside the cavity are simply proportional to those inside the cavity. For example:

$$\langle A_l^{\dagger\,\rm out}(\mathbf{k})A_l^{\rm out}(\mathbf{k}')\rangle = 2\gamma_l\langle A_l^\dagger(\mathbf{k})A_l(\mathbf{k}')\rangle, \tag{18}$$

so that normally ordered correlations in the Fourier plane, as (17) represent (apart from scaling factors) correlations in the far-field plane. In the ideal case of perfect translation symmetry in the transverse direction, as we consider here, the far field plane is located at an infinite distance from the cavity mirrors. However, it can be carried to a finite distance by placing a lens at a distance from the cavity equal to its focal length. Of course, the presence of the lens breaks the translational symmetry and introduces an axis for the system.

The analytical derivation of the intracavity correlation functions is performed in the Appendix A. In particular, from equation (85) we obtain:

$$\langle A_l^\dagger(\mathbf{k})A_l(\mathbf{k}')\rangle = \langle\beta_l(\mathbf{k})\beta_l^*(\mathbf{k}')\rangle - \frac{1}{2}\delta(\mathbf{k}-\mathbf{k}') = \frac{\gamma_p}{\gamma_l+\gamma_p}\left(\frac{|\mathcal{A}_0|^2}{1+\sigma_k^2-|\mathcal{A}_0|^2}\right)\delta(\mathbf{k}-\mathbf{k}'), \tag{19}$$

where

$$\sigma_k = \Delta + \frac{\gamma_l a_l + \gamma_p a_p}{\gamma_l+\gamma_p}\,k^2, \tag{20}$$

and from now on we consider $l = 1,2$ with $p = l+1\ (\mathrm{mod}\,2)$.

The far-field mean intensities outside the cavity of the signal ($l = 1$) and idler ($l = 2$) are obtained from the correlation functions (19) for $\mathbf{k}' = \mathbf{k}$, and are given by

$$\langle A_l^{\dagger\,\rm out}(\mathbf{k})A_l^{\rm out}(\mathbf{k})\rangle = 2\frac{\gamma_l\gamma_p}{\gamma_l+\gamma_p}\left(\frac{|\mathcal{A}_0|^2}{1+\sigma_k^2-|\mathcal{A}_0|^2}\right)\delta(0). \tag{21}$$

The factor $\delta(0)$ comes from the fact that, in the flat pump model, the signal field fluctuations in the transverse plane do not vanish for $|\mathbf{x}|\to\infty$ so that their Fourier transform are singular. It is however possible to remove such singular behaviour [26] by considering a screen with an aperture of linear size $d_{\rm A}$ immediately outside the input/output cavity mirror, and a lens at a focal distance f from the screen, as shown by Figure 1. In this case the field on the lens focal plane P_2 is given by:

$$\overline{B}_l(\mathbf{y}) = \frac{2\pi}{\mathrm{i}\lambda_l f}\int \mathrm{d}^2\mathbf{k}\ A_l^{\rm out}(\mathbf{k})R\left(\mathbf{k}-\frac{2\pi\mathbf{y}}{\lambda_l f}\right) + B_{\rm vac}(\mathbf{y}), \tag{22}$$

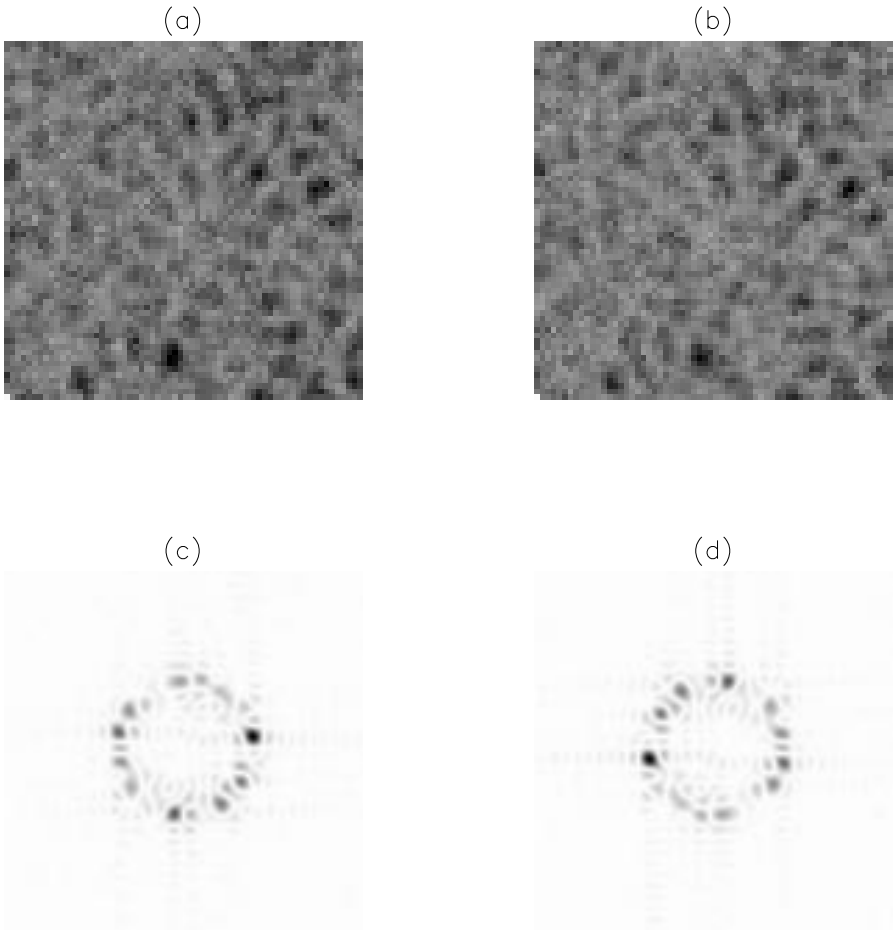

Fig. 2. Time average of the intensity of the signal and idler fluctuations for $\mathcal{A}_0 = 0.99$, and $\Delta = -1$. (a) Signal near-field, (b) idler near-field, (c) signal far-field (Fourier plane) and (d) idler far-field. The intensity is represented in grey scale, higher intensity corresponding to darker areas.

where λ_l is the field wavelength and

$$R(\mathbf{s}) = \frac{1}{4\pi^2}\int_Q \mathrm{d}^2\mathbf{x}\,\exp(\mathbf{s}\cdot\mathbf{x}) \tag{23}$$

is the response of the optical scheme, with Q being the area of the aperture. B_{vac} is an operator which accounts for vacuum fluctuation originating from the screen; this term is necessary to preserve field commutation relations, but it gives no contribution to the normally ordered field expectation values. In order to simplify notation we consider:

$$B_l(\mathbf{q}) = \frac{\mathrm{i}\lambda_l f}{2\pi}\overline{B}_l\left(\frac{2\pi\mathbf{y}}{\lambda_l f}\right)\cdot \tag{24}$$

Note that in the limit of an infinite aperture $Q \to \infty$, $R(\mathbf{s}) \to \delta(\mathbf{s})$, and $B_l(\mathbf{q}) \to A_l^{\mathrm{out}}(\mathbf{q})$, so that the field at the focal plane P_2 simply coincides with the spatial Fourier transform of the field immediately outside the cavity. In the following we shall however consider a large but *finite* aperture, in order to get rid of the artificial divergence in equation (21). In fact, in the limit where the diffraction spread $2\pi/d_{\mathrm{A}}$ from the aperture is small compared to the characteristic scale of variation of the correlation functions in the Fourier domain (that is, the scale of variation of quantity inside brackets at r.h.s. of (19)), equation (21) is replaced by

$$\langle B_l^\dagger(\mathbf{q})B_l(\mathbf{q})\rangle = \frac{Q}{4\pi^2}\frac{2\gamma_l\gamma_p}{(\gamma_l+\gamma_p)}\left(\frac{|\mathcal{A}_0|^2}{1+\sigma_q^2-|\mathcal{A}_0|^2}\right) \tag{25}$$

where the $\delta(0)$ has been replaced by a quantity proportional to the aperture area Q. For clarity reasons we present in the following several results concerning the far field correlation functions with and without the aperture that helps to remove divergencies from the final formulas.

The analytical expression of the mean far-field intensity is similar to that of the DOPO [14]; the mean intensities of signal and idler in the far-field are non-homogeneous, and display cylindrical symmetry around the mean direction of propagation. The intensity distributions present a maximum for $\sigma_k = 0$ *i.e.* for $|k|^2 = |k_{\mathrm{c}}|^2$ with k_{c} given by (7) the magnitude of the wave vector of the pattern above threshold for $\Delta < 0$. Since equation (21) depends only on $|k|^2$, the Fourier-plane intensity distributions of both signal and idler waves for $\Delta < 0$ are rings of radius defined by equation (7). In the physical far-field plane P_2 the intensity distributions of the two fields are two rings of radius $r_1 = |k_{\mathrm{c}}|\lambda_1 f/2\pi$ (signal), and $r_2 = |k_{\mathrm{c}}|\lambda_2 f/2\pi$ (idler).

This is confirmed by the numerical integration of equations (13) as shown in Figures 2c and 2d. As threshold is approached the peak intensity of the far field for both

signal and idler fields increases and the rings become narrower and narrower around the critical radius.

As far as the signal and idler intensities in the near-field are concerned, the situation is quite different. Indeed, we can show that the average intensities in the near field are spatially homogeneous. By transforming back in the real space equation (19) and using (14) we obtain

$$\begin{aligned}\langle A_l^{\dagger\,\mathrm{out}}(\mathbf{x})A_l^{\mathrm{out}}(\mathbf{x}')\rangle &= 2\gamma_l\left[\langle \Delta\alpha_l^*(\mathbf{x})\Delta\alpha_l(\mathbf{x}')\rangle - \frac{1}{2}\delta(\mathbf{x}-\mathbf{x}')\right] \\ &= \frac{1}{2\pi^2}\int \mathrm{d}^2\mathbf{k}\frac{\gamma_l\gamma_p}{\gamma_l+\gamma_p}\frac{|\mathcal{A}_0|^2}{1+\sigma_k^2-|\mathcal{A}_0|^2}\mathrm{e}^{\mathrm{i}\mathbf{k}\cdot(\mathbf{x}-\mathbf{x}')} \\ &= \frac{2}{\pi}\frac{\gamma_l\gamma_p}{\gamma_l+\gamma_p}\frac{\mathcal{A}_0^2}{\sqrt{1-\mathcal{A}_0^2}}\ \mathrm{Im}(K_0(-\mathrm{i}P|\mathbf{x}-\mathbf{x}'|)), \quad (26)\end{aligned}$$

where

$$P = \sqrt{k_c^2 + \mathrm{i}(1-|\mathcal{A}_0|^2)^{1/2}}, \quad (27)$$

and K_0 is the modified Bessel function of zero order. This the analogous of the result for the DOPO case discussed in [14].

From equation (26), it is clear that the average intensity in the near field is homogeneous since the right hand side of equation (26) does not depend of $\mathbf{x}$ when $\mathbf{x}=\mathbf{x}'$. This is confirmed by the numerical integration of the equations (13). Figures 2a and 2b are noisy and no spatial structure is observable; for an infinite integration time the signal and idler intensities are spatially uniform.

Up to this point, the analytical and numerical results are identical for both the degenerate and non degenerate cases, and from the analysis of the mean intensities there is no way to recognise the different nature of the patterns (travelling or standing wave) that appear above threshold in the two cases.

Although the ring in the average intensities in the far-field is generated by quantum fluctuations it is not a non-classical phenomenon but a generic feature of spatially extended and pattern forming systems in the presence of noise. Indeed, any noise drives these kind of systems to fluctuate away from their uniform state the closer one moves to the threshold of pattern formation. This phenomenon has been observed, for example, below the onset of Rayleigh-Bénard convection where the noise is due to thermal fluctuations [27]. In the specific case of the NDOPO, the far-field ring indicates that the near-field can be considered as the superimposition of traveling waves with many different orientations. As we pointed out earlier, the final orientation of the TWs above threshold is due only to the initial condition and the effect of noise below threshold is to continuously reset such initial condition.

It is then clear that we need more sophisticated tools to analyse and characterise the non-classical behaviour of spatially extended NDOPOs below threshold. It is for this reason that we study intensity and cross-correlation functions next.

4 Intensity and cross-correlation functions

In the case of the NDOPO, homodyne detection would require the use of two local oscillators, which is difficult to implement experimentally. To circumvent this drawback one could use a heterodyne detection with only one local oscillator. This method, however, requires the signal and idler frequencies to be very close together, a regime where our models are not accurate. We then consider the direct detection of the field intensities which requires no local oscillators and can be achieved using photocounting techniques.

We consider both the spatial correlation of intensity fluctuations for signal and idler taken separately, and the cross-correlation between signal and idler intensity fluctuations. The spatial correlation functions allow us to underline the differences between the degenerate and the non degenerate cases. Moreover, we show that purely quantum effects are detectable thanks to cross-correlation between signal and idler waves.

We start by considering the correlation functions of the signal (idler) intensity fluctuations at two different spatial points. The calculation of the intensity correlation functions is simplified by taking into account the Gaussian nature of the fluctuations in the Langevin equations. This allows us to express higher order moments by mean of second order moments of the fields. For the normally ordered intensity correlation (designed by a tilde) we obtain in the near-field:

$$\begin{aligned}\tilde{\Gamma}_{ll}(\mathbf{x},\mathbf{x}',\tau=0) &= \langle A_l^{\dagger\,\mathrm{out}}(\mathbf{x})A_l^{\dagger\,\mathrm{out}}(\mathbf{x}')A_l^{\mathrm{out}}(\mathbf{x}')A_l^{\mathrm{out}}(\mathbf{x})\rangle \\ &\quad - \langle A_l^{\dagger\,\mathrm{out}}(\mathbf{x})A_l^{\mathrm{out}}(\mathbf{x})\rangle\langle A_l^{\dagger\,\mathrm{out}}(\mathbf{x}')A_l^{\mathrm{out}}(\mathbf{x}')\rangle \\ &= \left|\langle A_l^{\mathrm{out}}(\mathbf{x})A_l^{\mathrm{out}}(\mathbf{x}')\rangle\right|^2 + \left|\langle A_l^{\dagger\,\mathrm{out}}(\mathbf{x})A_l^{\mathrm{out}}(\mathbf{x}')\rangle\right|^2, \quad (28)\end{aligned}$$

with $l=1,2$ and $\tau = t-t' = 0$ indicating that the correlations are taken at equal times. Similarly in the far-field the normally ordered intensity correlation function is given by:

$$\begin{aligned}&\tilde{G}_{ll}(\mathbf{k},\mathbf{k}',\tau=0) = \\ &\qquad \left|\langle A_l^{\mathrm{out}}(\mathbf{k})A_l^{\mathrm{out}}(\mathbf{k}')\rangle\right|^2 + \left|\langle A_l^{\dagger\,\mathrm{out}}(\mathbf{k})A_l^{\mathrm{out}}(\mathbf{k}')\rangle\right|^2. \quad (29)\end{aligned}$$

We note that the numerical simulations are performed by integrating the Langevin equations (13) for the intracavity fields, which are in the Wigner representation; therefore the numerical results correspond to symmetrical ordering and concern intracavity field correlations. Normally ordered correlations of the output fields (correlation functions with the tilde) are obtained from the numerical ones by using the combination of equations (16, 18).

4.1 Correlations in the far field

We calculate the intensity correlation function in the far-field outside the cavity using equation (21), and the fact

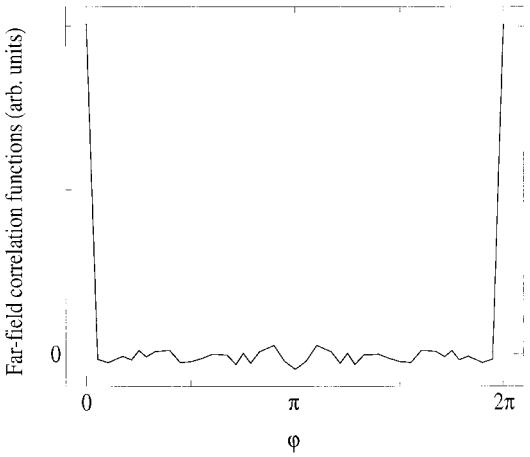

Fig. 3. Far-field (Fourier plane) correlation functions of the signal intensity *versus* the polar angle that spans the circle of Figure 2a for $k^2 = -\Delta = 1$ and $\mathcal{A}_0 = 0.99$.

that $\langle \beta_l(\mathbf{k})\beta_l(\mathbf{k}')\rangle = 0$ (see Eq. (84) in the Appendix A). We obtain:

$$\tilde{G}_{ll}(\mathbf{k},\mathbf{k}',\tau=0) = \left[2\gamma_l\left(\langle\beta_l(\mathbf{k})\beta_l^*(\mathbf{k}')\rangle - \frac{1}{2}\delta(\mathbf{k}-\mathbf{k}')\right)\right]^2 = g_{ll}(\mathbf{k})\,\delta^2(\mathbf{k}-\mathbf{k}') \tag{30a}$$

$$\tilde{G}_{ll}(\mathbf{q},\mathbf{q}',\tau=0) = \frac{Q}{4\pi^2}R(\mathbf{q}-\mathbf{q}')\,g_{ll}(\mathbf{q}), \tag{30b}$$

where we have defined

$$g_{ll}(\mathbf{k}) = 4\left(\frac{\gamma_l\gamma_p\,|\mathcal{A}_0|^2}{(\gamma_l+\gamma_p)\,(1+\sigma_k^2-|\mathcal{A}_0|^2)}\right)^2. \tag{31}$$

Equation (30b) has been obtained by considering the far-field formed by the aperture and the lens arrangement shown in Figure 1, and for $g_{ll}(\mathbf{q})$ varying on a scale much slower than the diffraction spread $2\pi/d_{\rm A}$ from the aperture; in this case the function $R(\mathbf{q}-\mathbf{q}')$ at r.h.s. constitutes a finite approximation for a Dirac delta function, so that equation (30b) represents the *finite* equivalent of equation (30a).

When moving the two detectors on the far-field circle of either signal or idler field, the single field (signal or idler) intensity correlation function displays one Dirac peak for $\mathbf{k} = \mathbf{k}'$ (self correlation). In Figure 3, we have plotted the results of the numerical simulation for the correlation functions (30a). Both $\mathbf{k}$ and $\mathbf{k}'$ lie on the critical circle, and ϕ is the azimuthal angle between the two wave vectors. The correlation functions are obtained by performing a time average plus an average with respect to the position of one detector over the circle.

This result is different from that obtained in the case of the DOPO [14]. We recall that in the degenerate case, the correlation function on the far-field circle shows two Dirac peaks, one for $\mathbf{k} = \mathbf{k}'$ ($\phi = 0$), and one for $\mathbf{k} = -\mathbf{k}'$ ($\phi = \pi$). The interpretation is simple: in the degenerate OPO, one pump photon is converted into two twin signal photons which are emitted along two symmetrical off-axis direction in order to preserve the transverse momentum.

In the NDOPO, one pump photon is converted into one signal and one idler photon. If an intensity (or photocount) detection is performed at just one of the frequencies (which is often the case experimentally), then there is no twin photons present at 180° on the far field circle. The intensity correlation functions in the far-field are then capable to underline the difference between the degenerate and the non degenerate cases. Two peaks in the intensity correlation function of the far-field circle correspond to a standing wave pattern above threshold (rolls in the DOPO [14]) while a single peak in the same correlation function (see Fig. 3) corresponds to travelling wave pattern above threshold for the field under consideration. In both cases, the use of quantum images below threshold allows one to characterise the type of pattern appearing above threshold.

We now calculate the intensity correlation function between signal and idler (cross-correlation), and find:

$$\tilde{G}_{lp}(\mathbf{k},\mathbf{k}',\tau=0) = 4\gamma_l\gamma_{\rm p}\langle\beta_l(\mathbf{k})\beta_p(\mathbf{k}')\rangle\langle\beta_l^*(\mathbf{k})\beta_p^*(\mathbf{k}')\rangle = g_{lp}(\mathbf{k})\,\delta^2(\mathbf{k}+\mathbf{k}'), \tag{32a}$$

$$\tilde{G}_{lp}(\mathbf{q},\mathbf{q}',\tau=0) = \frac{Q}{4\pi^2}R(\mathbf{q}+\mathbf{q}')g_{lp}(\mathbf{q}) \qquad l,p=1,2,\ l\neq p \tag{32b}$$

with

$$g_{lp}(\mathbf{k}) = 4\left(\frac{\gamma_l\gamma_p}{\gamma_l+\gamma_p}\right)^2 \times\left(\frac{|\mathcal{A}_0|^2}{1+\sigma_k^2-|\mathcal{A}_0|^2}+\frac{|\mathcal{A}_0|^4}{(1+\sigma_k^2-|\mathcal{A}_0|^2)^2}\right). \tag{33}$$

where we have used the fact that $\langle\beta_l(\mathbf{k})\beta_p^*(\mathbf{k}')\rangle = 0$ (see Eq. (87) in Appendix A). Note that in this case, the normally ordered and symmetrically ordered components are equal. The cross-correlation function is plotted in Figure 4. $G_{lp}(\mathbf{k},\mathbf{k}')$ displays only one positive peak for $\phi = \pi$. This is a clear evidence of the fact that the idler and signal photons are emitted with opposite transverse momenta $\mathbf{k}$ and $-\mathbf{k}$. Note that there is no correlation peak for $\phi = 0$ since there is only one photon at a time either in the signal or in the idler field.

More importantly, a comparison of equations (33, 31) clearly shows that the cross-correlation peak at $\mathbf{k}' = -\mathbf{k}$ is larger than the self-correlation peak at $\mathbf{k}' = \mathbf{k}$. This cannot be obtained by a light field with classical statistics, for which the Glauber P-representation exists and is strictly positive. In this case, the normally ordered correlation function (32a) can be written in the form:

$$\tilde{G}_{lp}(\mathbf{k},\mathbf{k}',\tau=0) = \langle\delta i_l(\mathbf{k})\,\delta i_{\rm p}(\mathbf{k}')\rangle_{\rm P}, \tag{34}$$

where $\delta i_l(\mathbf{k})$ is the c-number distribution that in the P-representation correspond to the intensity fluctuation operator for the lth field, and $\langle\ \rangle_{\rm P}$ is the classical-looking average over the P-functional. The quantity at r.h.s. of (34) is an inner product and the Schwarz inequality

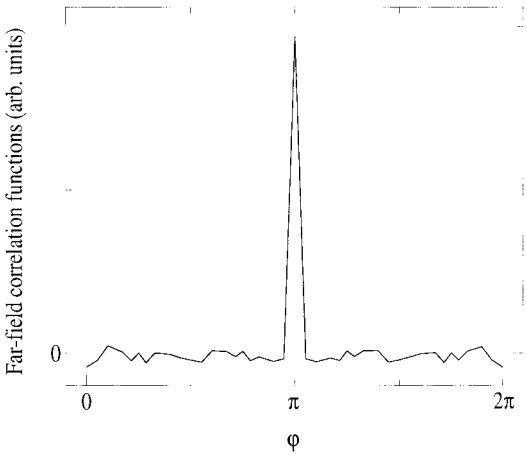

Fig. 4. Far-field (Fourier-plane) correlation functions between signal and idler intensities. The parameters are the same as in Figure 3.

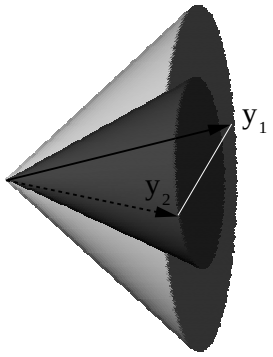

Fig. 5. Schematic view of the twin photon emission in the NDOPO. Signal and idler photons are emitted with opposite transverse wavevectors, and propagate along two cones, whose intersection with the far field plane is shown in the figure. Two detectors placed around the conjugate positions $\mathbf{y}_1$, $\mathbf{y}_2$ measure perfectly correlated photocounts.

imposes that:

$$|\langle \delta i_l(\mathbf{k})\, \delta i_p(\mathbf{k}')\rangle_{\mathrm{P}}|^2 \leq \langle \delta i_l(\mathbf{k})\, \delta i_l(\mathbf{k})\rangle_{\mathrm{P}}\ \langle \delta i_p(\mathbf{k}')\, \delta i_p(\mathbf{k}')\rangle_{\mathrm{P}} = \tilde{G}_{ll}(\mathbf{k},\mathbf{k})\, \tilde{G}_{pp}(\mathbf{k}',\mathbf{k}'). \quad (35)$$

When specialised to the case $\mathbf{k}' = -\mathbf{k}$, the inequality (35) implies that

$$g_{lp}(\mathbf{k}) \leq g_{ll}(\mathbf{k}). \quad (36)$$

We can therefore conclude that a cross-correlation between signal and idler intensity fluctuations larger than each of the self-correlations has no classical counterpart when considering coherent states as the boundary between classical and non-classical states of the radiation. Note that this argument is similar to that which leads to the definition of antibunching in the time domain.

Moreover, the violation of the classical Cauchy-Schwartz inequality implied by equations (31, 33) is the largest possible: signal and idler intensity fluctuations at two opposite transverse wavevectors are perfectly correlated, in such a way that the difference between photon numbers collected at the two conjugate positions $\mathbf{y}_1 = \mathbf{k}\,(\lambda_1 f)/(2\pi)$, $\mathbf{y}_2 = -\mathbf{k}\,(\lambda_2 f)/(2\pi)$ in the far-field plane of signal and idler (see Fig. 5), is a noiseless observable.

In order to prove this last statement, the model for a nondegenerate OPO has been reformulated in the framework of cavity input/output formalism. Below threshold, where pump depletion can be neglected, and in the absence of losses, output signal and idler field operators are linked to the input ones by a linear transformation of the form:

$$A_1^{\mathrm{out}}(\mathbf{k},\omega) = U_1(\mathbf{k},\omega)A_1^{\mathrm{in}}(\mathbf{k},\omega) + V_1(\mathbf{k},\omega)A_2^{\dagger\,\mathrm{in}}(-\mathbf{k},-\omega),$$
$$A_2^{\mathrm{out}}(\mathbf{k},\omega) = U_2(\mathbf{k},\omega)A_2^{\mathrm{in}}(\mathbf{k},\omega) + V_2(\mathbf{k},\omega)A_1^{\dagger\,\mathrm{in}}(-\mathbf{k},-\omega), \quad (37)$$

where ω represents the frequency shift from the carrier frequencies and $\mathbf{k}$ the transverse wavevector. The explicit form of the functions U_i, V_i is given in Appendix B. For our purposes, however, the only relevant point is the unitarity of the transformation (37), which implies that functions U_i, V_i satisfy the following requirements:

$$|U_i(\mathbf{k},\omega)|^2 - |V_i(\mathbf{k},\omega)|^2 = 1 \qquad (i=1,2), \quad (38)$$
$$U_1(\mathbf{k},\omega)V_2(-\mathbf{k},-\omega) - V_1(\mathbf{k},\omega)U_2(-\mathbf{k},-\omega) = 0. \quad (39)$$

From the conditions (38, 39), it also follows that

$$|V_1(\mathbf{k},\omega)|^2 = |V_2(-\mathbf{k},-\omega)|^2, \quad (40)$$

a mathematical relation that will be useful in the following.

By making use of the fact that the input fields are in the vacuum state, the mean intensity distributions in the Fourier plane are calculated as:

$$\langle I_i(\mathbf{k},t)\rangle = \langle A_i^{\dagger\,\mathrm{out}}(\mathbf{k},t)A_i^{\mathrm{out}}(\mathbf{k},t)\rangle = \delta(0)\int\frac{\mathrm{d}\omega}{2\pi}\,|V_i(\mathbf{k},\omega)|^2 \quad (41a)$$

$$\langle I_i(\mathbf{q},t)\rangle = \frac{Q}{4\pi^2}\int\frac{\mathrm{d}\omega}{2\pi}\,|V_i(\mathbf{q},\omega)|^2 \qquad (i=1,2). \quad (41b)$$

Hence expression (40) expresses just the fact that the mean number of signal photons emitted by the cavity per unit time at the wavevector $\mathbf{k}$ equals that of idler photons at the symmetrical wavevector $-\mathbf{k}$.

We are here interested in correlation functions of intensity fluctuations at different times in the Fourier plane (far-field plane) of the form:

$$\tilde{G}_{ij}(\mathbf{k},\mathbf{k}',\tau=t) = \langle :\ \delta I_i(\mathbf{k},t)\, \delta I_j(\mathbf{k}',0)\ :\rangle \ \text{ with}$$
$$\delta I_i(\mathbf{k},t) = A_i^{\dagger\,\mathrm{out}}(\mathbf{k},t)A_i^{\mathrm{out}}(\mathbf{k},t) - \langle A_i^{\dagger\,\mathrm{out}}(\mathbf{k},t)A_i^{\mathrm{out}}(\mathbf{k},t)\rangle \qquad (i,j=1,2), \quad (42)$$

where : : indicate normal ordering, and in their spectra:

$$\tilde{G}_{ij}(\mathbf{k},\mathbf{k}',\omega) = \int_{-\infty}^{+\infty}\mathrm{d}t\,\mathrm{e}^{-\mathrm{i}\omega t}\langle :\ \delta I_i(\mathbf{k},t)\, \delta I_j(\mathbf{k}',0)\ :\rangle. \quad (43)$$

As outlined in Appendix B the correlation functions (43) can be calculated in terms of functions U_i, V_i as:

$$\tilde{G}_{ij}(\mathbf{k},\mathbf{k}',\omega) = \delta_{ij}[\delta(\mathbf{k}-\mathbf{k}')]^2 \int \frac{\mathrm{d}\omega'}{2\pi} \left|V_i(\mathbf{k},\omega')\right|^2 \left|V_j(\mathbf{k},\omega'-\omega)\right|^2 + (1-\delta_{ij})[\delta(\mathbf{k}+\mathbf{k}')]^2 \int \frac{\mathrm{d}\omega'}{2\pi} U_i(\mathbf{k},\omega')U_i^*(\mathbf{k},\omega'-\omega) \times V_j(-\mathbf{k},-\omega')V_j^*(-\mathbf{k},-\omega'+\omega) \quad (44a)$$

$$\tilde{G}_{ij}(\mathbf{q},\mathbf{q}',\omega) = \delta_{ij}\frac{Q}{4\pi^2}R(\mathbf{q}-\mathbf{q}') \int \frac{\mathrm{d}\omega'}{2\pi} \left|V_i(\mathbf{q},\omega')\right|^2 \left|V_j(\mathbf{q},\omega'-\omega)\right|^2 + (1-\delta_{ij})\frac{Q}{4\pi^2}R(\mathbf{q}+\mathbf{q}') \int \frac{\mathrm{d}\omega'}{2\pi} U_i(\mathbf{q},\omega')U_i^*(\mathbf{q},\omega'-\omega) \times V_j(-\mathbf{q},-\omega')V_j^*(-\mathbf{q},-\omega'+\omega). \quad (44b)$$

As for the equal time correlations, when intensity fluctuations of the signal (idler) alone are considered, there is a single correlation peak located at $\mathbf{k}=\mathbf{k}'$; the cross-correlation between signal and idler presents a single peak at $\mathbf{k}=-\mathbf{k}'$.

At low frequencies (that corresponds to integrating the two-times correlation over long times) we have:

$$\tilde{G}_{ii}(\mathbf{k},\mathbf{k}',\omega=0) = [\delta(\mathbf{k}-\mathbf{k}')]^2 \int \frac{\mathrm{d}\omega'}{2\pi} \left|V_i(\mathbf{k},\omega')\right|^4 \quad (45a)$$

$$\tilde{G}_{ii}(\mathbf{q},\mathbf{q}',\omega=0) = \frac{Q}{4\pi^2}R(\mathbf{q}-\mathbf{q}') \int \frac{\mathrm{d}\omega'}{2\pi} \left|V_i(\mathbf{q},\omega')\right|^4 \quad (i=1,2), \quad (45b)$$

while for $i \neq j$:

$$\tilde{G}_{ij}(\mathbf{k},-\mathbf{k}',\omega=0) = [\delta(\mathbf{k}-\mathbf{k}')]^2 \int \frac{\mathrm{d}\omega'}{2\pi} \left|U_i(\mathbf{k},\omega')V_j(-\mathbf{k},-\omega)\right|^2 \quad (46a)$$

$$= [\delta(\mathbf{k}-\mathbf{k}')]^2 \int \frac{\mathrm{d}\omega'}{2\pi} \left[1+\left|V_i(\mathbf{k},\omega')\right|^2\right] \left|V_i(\mathbf{k},\omega)\right|^2 \quad (46b)$$

$$= \tilde{G}_{ii}(\mathbf{k},\mathbf{k}',\omega=0) + \delta(\mathbf{k}-\mathbf{k}')\langle I_i(\mathbf{k},t)\rangle \quad (46c)$$

$$\tilde{G}_{ij}(\mathbf{q},-\mathbf{q}',\omega=0) = \tilde{G}_{ii}(\mathbf{q},\mathbf{q}',\omega=0) + R(\mathbf{q}-\mathbf{q}')\langle I_i(\mathbf{q},t)\rangle, \quad (46d)$$

where, in passing from (46a) to (46b) we made use of the two unitarity conditions (40, 38); the third line follows directly from (45b) and from the expression of the mean intensity (41b).

We are now ready to discuss our result: let us consider the far-field plane (see again Fig. 5 for reference) and two detectors measuring the photon flux at the signal frequency crossing a region S_1 around the position $\mathbf{y}_1 = \mathbf{k}\,(\lambda_1 f)/(2\pi)$, and the photon flux at the idler frequency crossing a region S_2 around the conjugate position $\mathbf{y}_2 = -\mathbf{k}\,(\lambda_2 f)/(2\pi)$, for some wavevector $\mathbf{k}$. In the Fourier plane this corresponds to considering the two observables

$$N_1(t) = \int_{S_1} \mathrm{d}\mathbf{k}'\, I_1(\mathbf{k}',t) \quad (47)$$

$$N_2(t) = \int_{S_2} \mathrm{d}\mathbf{k}'\, I_2(\mathbf{k}',t) \quad (48)$$

where S_1 and S_2 are two symmetric regions in the Fourier plane placed around the wavevectors $\mathbf{k}$ and $-\mathbf{k}$. Let us introduce the operator difference of photocounts

$$N_-(t) = N_1(t) - N_2(t), \quad (49)$$

and its noise spectrum

$$V_-(\omega) = \int_{-\infty}^{+\infty} \mathrm{d}t\, \mathrm{e}^{-\mathrm{i}\omega t}\langle \delta N_-(t)\delta N_-(0)\rangle \quad (50)$$

$$= (SN)_- + S_-(\omega). \quad (51)$$

In the last line, by using standard commutation relations of field operators, we have isolated in V_- the shot-noise contribution

$$(SN)_- = \int_{S_1} \mathrm{d}\mathbf{k}'\, \langle I_1(\mathbf{k}',t)\rangle + \int_{S_2} \mathrm{d}\mathbf{k}'\, \langle I_2(\mathbf{k}',t)\rangle, \quad (52)$$

which represents the level of noise that would be showed by the observable N_- if the two downconverted fields were emitted in coherent states (displaying no spatial correlation at all). The normally ordered part of the noise spectrum

$$S_-(\omega) = \int_{-\infty}^{+\infty} \mathrm{d}t\, \mathrm{e}^{-\mathrm{i}\omega t}\langle : \delta N_-(t)\delta N_-(0) : \rangle \quad (53)$$

hence represents the excess/reduction of noise with respect to the coherent state case.

By making use of the symmetry of regions S_2 and S_1, it can be easily verified that

$$S_-(\omega) = \int_{S_1} \mathrm{d}\mathbf{k}' \int_{S_1} \mathrm{d}\mathbf{k}'' \left\{\tilde{G}_{11}(\mathbf{k}',\mathbf{k}'',\omega) + \tilde{G}_{22}(-\mathbf{k}',-\mathbf{k}'',\omega) - \tilde{G}_{12}(\mathbf{k}',-\mathbf{k}'',\omega) - \tilde{G}_{21}(-\mathbf{k}',\mathbf{k}'',\omega)\right\}. \quad (54)$$

Finally, by taking into account the result (46c) for the cross-correlation between signal and idler, we obtain at zero frequency:

$$S_-(\omega=0) = -\int_{S_1} \mathrm{d}\mathbf{k}'\, \{\langle I_1(\mathbf{k}',t)\rangle + \langle I_2(-\mathbf{k}',t)\rangle\} = -(SN)_-, \quad (55)$$

that is,

$$V_-(0) = 0.$$

Hence the microscopic process of emission of twin photons with opposite transverse wavevectors manifests itself

as a perfect spatial correlation between portions of the two beams cross-sections in the far field. The result neither depends on the distance from threshold, nor on the position $\boldsymbol{\zeta}_1$ of the detector in the signal far field plane, provided the second detector is placed at the conjugate position, but depends only on the form of the input/output transformation (37). Actually the same kind of correlation is found in a cavityless parametric amplifier [28], and in a DOPO with a spherical mirror resonator [29].

4.2 Correlations in the near field

The intensity correlation functions in the near-field are obtained by transforming back in the real space the mathematical relations obtained in the far-field. For the signal (idler) intensity correlation function at equal times we have:

$$\tilde{\Gamma}_{ll}(\mathbf{x},\mathbf{x}',\tau=0)=\left(\frac{\gamma_l\gamma_p\,|\mathcal{A}_0|^2}{\pi(\gamma_l+\gamma_p)\,\sqrt{1-|\mathcal{A}_0|^2}}\times \mathrm{Im}K_0(-\mathrm{i}P|\mathbf{x}-\mathbf{x}'|)\right)^2. \quad (56)$$

The corresponding symmetrically ordered component is:

$$\Gamma_{ll}(\mathbf{x},\mathbf{x}',\tau=0)=\tilde{\Gamma}_{ll}(\mathbf{x},\mathbf{x}',\tau=0) + \delta(\mathbf{x}-\mathbf{x}')\left(\langle A_l^\dagger(\mathbf{x})A_l(\mathbf{x}')\rangle+\frac{1}{4}\delta(\mathbf{x}-\mathbf{x}')\right). \quad (57)$$

For the cross-correlation function between signal and idler we have (normally and symmetrically ordered components are equal):

$$\tilde{\Gamma}_{lp}(\mathbf{x},\mathbf{x}',\tau=0)=\frac{|\mathcal{A}_0|^2}{\pi^2}\left(\frac{\gamma_l\gamma_p}{\gamma_l+\gamma_p}\right)^2 \times\left[\left(\frac{1}{\sqrt{1-|\mathcal{A}_0|^2}}\mathrm{Im}K_0(-\mathrm{i}P|\mathbf{x}-\mathbf{x}'|)\right)^2 + \left(\mathrm{Re}K_0(-\mathrm{i}P|\mathbf{x}-\mathbf{x}'|)\right)^2\right]. \quad (58)$$

Both correlation functions (56, 58) are characterised by a modulation with respect to the distance $r=|\mathbf{x}-\mathbf{x}'|$ (alternation between correlation and anticorrelation). The wavelength of the modulation is half of that of the classical phase modulation $\lambda_c=2\pi/k_c$ appearing above threshold, and therefore can be considered as an anticipation of the incoming pattern. Note that the factor 1/2 for the wavelength comes form the fact that we are considering intensity correlations instead of field correlations. As for the case of far-field correlations, we have obtained excellent agreement between the analytical functions and the results of the numerical integration of the Langevin equations (9).

In the case of the NDOPO, the sum and difference of the signal and idler intensities are known to display interesting features, such as non classical effect for the intensity difference [30]. We here analyse the correlation functions of those quantities in the case of a spatially extended system. Since we are below threshold where the classical expectation values of the signal and idler fields are zero, these correlation functions correspond to the sum and difference of photo-counts between photo-counters at the frequencies of the signal and idler respectively. First, we consider the sum of the signal and idler intensities, this quantity as well as the difference can be expressed in term of self and cross-correlation of signal and idler. Indeed we have:

$$\tilde{\Gamma}_{\mathrm{sum}}(\mathbf{x},\mathbf{x}',\tau=0)=\langle:(I_1(\mathbf{x})+I_2(\mathbf{x}))(I_1(\mathbf{x}')+I_2(\mathbf{x}')):\rangle =\tilde{\Gamma}_{11}+\tilde{\Gamma}_{22}+\tilde{\Gamma}_{12}+\tilde{\Gamma}_{21}, \quad (59)$$

where

$$I_l(\mathbf{x})=A_l^{\dagger\,\mathrm{out}}(\mathbf{x})A_l^{\mathrm{out}}(\mathbf{x}),\qquad \text{with } l=1,2 \quad (60)$$

and : : indicate normal ordering. The correlation function of the sum of signal and idler intensities corresponds to the sum of self ($\tilde{\Gamma}_{ll}$) and cross-correlation functions ($\tilde{\Gamma}_{lp}$).

In the near field, we have:

$$\tilde{\Gamma}_{\mathrm{sum}}(\mathbf{x},\mathbf{x}',\tau=0)=2\frac{|\mathcal{A}_0|^2}{\pi^2}\left(\frac{\gamma_l\gamma_p}{\gamma_l+\gamma_p}\right)^2 \times\left[\frac{1+|\mathcal{A}_0|^2}{1-|\mathcal{A}_0|^2}\left(\mathrm{Im}K_0(-\mathrm{i}P|\mathbf{x}-\mathbf{x}'|)\right)^2 + \left(\mathrm{Re}K_0(-\mathrm{i}P|\mathbf{x}-\mathbf{x}'|)\right)^2\right]. \quad (61)$$

The curve of Figure 6 displays a modulation with maxima at half the wavelength of the pattern appearing at threshold. The explicit expression of the near-field correlation of the sum of signal and idler intensities is similar to the

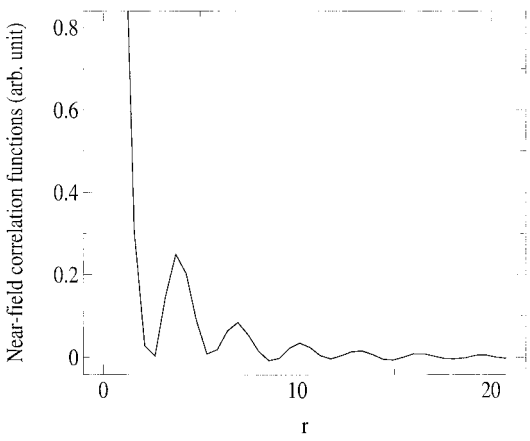

Fig. 6. Near-field correlation function for the sum of signal and idler intensities from the numerical simulations of the Langevin equations. When comparing it with the analytical result given by (61) the Dirac peak for $r=0$ disappears since (61) is normally ordered.

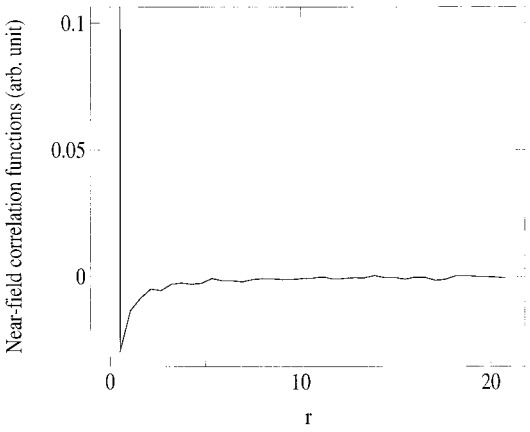

Fig. 7. Near-field correlation function for the difference between signal and idler intensities from the numerical simulations of the Langevin equations.

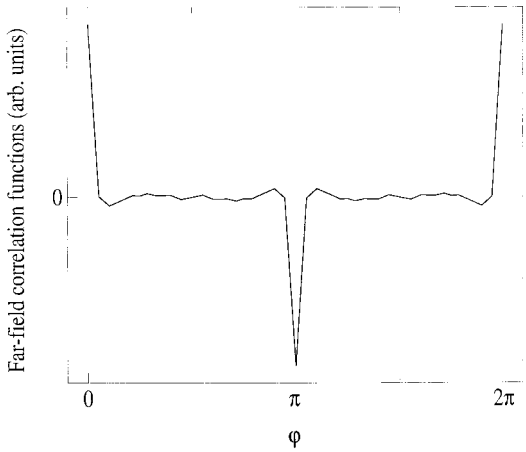

Fig. 8. Far-field correlation function for the difference between signal and idler intensities from the numerical simulations of the Langevin equations.

intensity correlation of the DOPO [14] and we can say that by measuring the sum of signal and idler intensities we recover the characteristics of the correlations of the degenerate OPO. However, we note that above threshold we do not observe a standing wave in the sum of signal and idler intensities. The sum of the intensities of the two fields displays no spatial modulation as already seen for its two components.

By using the cross-correlations between signal and idler fields, we have shown previously that the signal and idler photon are emitted simultaneously and with opposite transverse wavevector in order to preserve the momentum. We can therefore expect a reduction of the fluctuations on the difference between signal and idler intensities. In the near-field, the correlation functions for the intensity difference is:

$$\tilde{\Gamma}_{\rm diff}(\mathbf{x},\mathbf{x}',\tau=0) = \langle : (I_1(\mathbf{x}) - I_2(\mathbf{x}))(I_1(\mathbf{x}') - I_2(\mathbf{x}')) : \rangle = \tilde{\Gamma}_{11} + \tilde{\Gamma}_{22} - \tilde{\Gamma}_{12} - \tilde{\Gamma}_{21}. \quad (62)$$

This corresponds to the difference between self-correlation ($\tilde{\Gamma}_{ll}$) and cross-correlation ($\tilde{\Gamma}_{lp}$) functions. Therefore we have the following expression:

$$\tilde{\Gamma}_{\rm diff}(\mathbf{x},\mathbf{x}',\tau=0) = -2\frac{|\mathcal{A}_0|^2}{\pi^2}\left(\frac{\gamma_l\gamma_p}{\gamma_l+\gamma_p}\right)^2 \times \left|K_0(-\mathrm{i}P|\mathbf{x}-\mathbf{x}'|)\right|^2. \quad (63)$$

The normally ordered correlation functions is negative, a clear signature of squeezing (see Fig. 7). The squeezing effect comes from the simultaneous emission of photons in the signal and idler fields. When $\mathbf{x} \to \mathbf{x}'$, the normally ordered variance $\tilde{\Gamma}_{\rm diff}(\mathbf{x},\mathbf{x}',\tau=0) \to -\infty$. We note also that the correlation function displays no modulation with respect to $|\mathbf{x}-\mathbf{x}'|$. In this case, non-classical effects are separated from the modulation of the correlation function due to pattern formation.

4.3 Correlations for the sum and difference of intensities in the far field

Finally, for completeness, we briefly discuss the correlation functions for the sum and differences of signal and idler photons measured in separate positions in the far-field. These are, respectively,

$$\tilde{G}_{\rm sum}(\mathbf{k},\mathbf{k}',\tau=0) = (g_{11}(\mathbf{k}) + g_{22}(\mathbf{k}))\,\delta^2(\mathbf{k}-\mathbf{k}') + (g_{12}(\mathbf{k}) + g_{21}(\mathbf{k}))\,\delta^2(\mathbf{k}+\mathbf{k}') \quad (64a)$$

$$\tilde{G}_{\rm sum}(\mathbf{q},\mathbf{q}',\tau=0) = \frac{Q}{4\pi^2}\left[R(\mathbf{q}-\mathbf{q}')\,(g_{11}(\mathbf{q}) + g_{22}(\mathbf{q})) + R(\mathbf{q}+\mathbf{q}')\,(g_{12}(\mathbf{q}) + g_{21}(\mathbf{q}))\right] \quad (64b)$$

$$\tilde{G}_{\rm diff}(\mathbf{k},\mathbf{k}',\tau=0) = (g_{11}(\mathbf{k}) + g_{22}(\mathbf{k}))\,\delta(\mathbf{k}-\mathbf{k}') - (g_{12}(\mathbf{k}) + g_{21}(\mathbf{k}))\,\delta(\mathbf{k}+\mathbf{k}') \quad (65a)$$

$$\tilde{G}_{\rm diff}(\mathbf{q},\mathbf{q}',\tau=0) = (g_{11}(\mathbf{q}) + g_{22}(\mathbf{q}))\,R(\mathbf{q}-\mathbf{q}') - (g_{12}(\mathbf{q}) + g_{21}(\mathbf{q}))\,R(\mathbf{q}+\mathbf{q}') \quad (65b)$$

where $g_{ll}(\mathbf{k})$ and $g_{lp}(\mathbf{k})$ are given by equations (31, 33). Such correlation functions comprise two peaks, one for $\phi = 0$ and the second one for $\phi = \pi$. In the case of the sum of photon numbers both peaks are positive while for the differences between signal and idler photons the correlation function the peak for $\phi = 0$ is positive while the peak for $\phi = \pi$ is negative (see Fig. 8). The negative correlation peak of Figure 8 is clearly due to the cross-correlation term $g_{lp}(\mathbf{k})$ being larger than self-correlation contribution $g_{ll}(\mathbf{k})$. This corresponds to a strong (below shot noise limit) reduction in the fluctuations of the measured observable and the negative peak at $\phi = \pi$ is a clear non-classical aspect of NDOPO quantum images.

5 From below to above threshold

In the last section of this paper we consider the case of sampling the output signal of the NDOPO with a detector fast enough to resolve the quantum fluctuations responsible for the quantum image. This can be numerically achieved by using the nonlinear Langevin equations (9). Indeed, the numerical simulation of these equations can provide us snapshots of the signal intensity without unphysical divergences when crossing the threshold. By increasing the pump amplitude, we can analyse the transition from below to above threshold, and the transformation of the quantum image into the classical pattern. We focus here on the triply resonant configuration but similar results are obtained also for the doubly resonant case.

Figure 9 displays snapshots obtained by varying the pump amplitude from below to above threshold. The left column shows the real part distribution of the signal field, the central column the intensity distribution its near-field, and the right one the intensity distribution of its far-field.

Well below threshold the signal is completely noisy both in the near and in the far-field. When one gets closer to the threshold, the signal acquires an increasing level of spatial order. Below threshold (see Fig. 9b) the snapshot exhibits the formation of spot patterns in the near field. These spots have a slow random motion which produces a zero value for the averaged signal near-field. However, we know from the previous sections that the size and distribution of spots is not completely random since the probability of finding two spots separated by the distance r has a maxima when r is a multiple of the critical wavelength $\lambda_{\rm c}$ which characterises the modulation of the traveling wave that appears above threshold. The far-field intensity distribution is concentrated on the circle of radius equal to the modulus of the critical wave vector $k_{\rm c} = 2\pi/\lambda_{\rm c}$, (see Fig. 9c). The system tends to form traveling waves, but the orientation is continuously mixed. Above threshold, stripes are visible in the real part of the near field pattern in Figure 9. The far-field corresponding to this situation is a single bright spot (Fig. 9) off optical axes. Note that at difference with the DOPO case, the signal intensity displays no stripe structure since the pattern is a traveling wave [17].

6 Conclusions

We have shown, both numerically and analytically, that the classical phase pattern arising above threshold in a NDOPO is anticipated by the far-field quantum correlation function of intensity fluctuations (quantum image).

Moreover, thanks to the nonlinear Langevin equation, we have been able to follow the transformation from the quantum image into the classical one. In addition to the critical wavenumber of the pattern appearing at threshold, the quantum image provides information about the type of pattern, *i.e.* traveling wave for a NDOPO, standing wave for a DOPO. The feature of quantum images to anticipate the pattern appearing at threshold motivate further investigation in more complex situation, for example in the presence of squares or hexagons [22].

Non-classical features such as squeezing below the shot-noise have been recovered in the cross-correlation functions involving photo-counts of both signal and idler fields. We have showed that there exist a high level of spatial correlation between the idler and signal beam cross-sections in the far field plane: intensity fluctuations in whatever pair of conjugate portions of the two beams are perfectly correlated, in such a way that the difference of photocounts detected from the two portions is (ideally) a noiseless observable.

We would like to thank Claude Fabre, Steve Barnett and John Jeffers for useful discussions. This work has been supported by the European Union Training and Mobility of Researcher programme (Network Quantum Structures, contract No. FMRXCT960077) and, in part, by EPSRC (grants GR/K70212 and GR/M19727).

Appendix A

The linear stochastic differential equations (13) allows for analytical solutions of the correlations functions in the Fourier space. The Fourier transform of the equations (13) and its conjugate are written in a convenient matrix form:

$$\frac{\partial}{\partial t}\begin{pmatrix}\beta_l(\mathbf{k},t)\\ \beta_p^*(-\mathbf{k},t)\end{pmatrix} = \begin{pmatrix}-\gamma_l(1+\mathrm{i}\sigma_{lk}) & \sqrt{\gamma_l\gamma_p}\mathcal{A}_0\\ \sqrt{\gamma_l\gamma_p}\mathcal{A}_0^* & -\gamma_p(1-\mathrm{i}\sigma_{pk})\end{pmatrix} \times \begin{pmatrix}\beta_l(\mathbf{k},t)\\ \beta_p^*(-\mathbf{k},t)\end{pmatrix} + \sqrt{2}\begin{pmatrix}\sqrt{\gamma_l}\eta_l(\mathbf{k},t)\\ \sqrt{\gamma_p}\eta_p^*(-\mathbf{k},t)\end{pmatrix}, \quad (66)$$

where $l = 1, 2,\ p = 3 - l$ and where we have introduced the wave-vector dependent detuning

$$\sigma_{lk} = \Delta + a_l k^2, \qquad \sigma_{pk} = \delta_p + a_p k^2. \quad (67)$$

The Fourier transform of the Langevin forces satisfy

$$\langle \eta_l^*(-\mathbf{k},t)\eta_p(\mathbf{k}',t')\rangle = \frac{1}{2}\delta(\mathbf{k}-\mathbf{k}')\delta(t-t')\delta_{lp} \quad (68a)$$

$$\langle \eta_l(\mathbf{k},t)\eta_p(\mathbf{k}',t')\rangle = 0. \quad (68b)$$

Equation (66) describes the stochastic dynamics of the field fluctuations in the far-field. The formal solution of equation (66) is given by:

$$\begin{pmatrix}\beta_l(\mathbf{k},t)\\ \beta_p^*(-\mathbf{k},t)\end{pmatrix} = \mathrm{e}^{Mt}\begin{pmatrix}\beta_l(\mathbf{k},0)\\ \beta_p^*(-\mathbf{k},0)\end{pmatrix} + \sqrt{2}\mathrm{e}^{Mt}\int_0^t \mathrm{d}t'\mathrm{e}^{-Mt'}\begin{pmatrix}\sqrt{\gamma_l}\eta_l(\mathbf{k},t')\\ \sqrt{\gamma_p}\eta_p^*(-\mathbf{k},t')\end{pmatrix}, \quad (69)$$

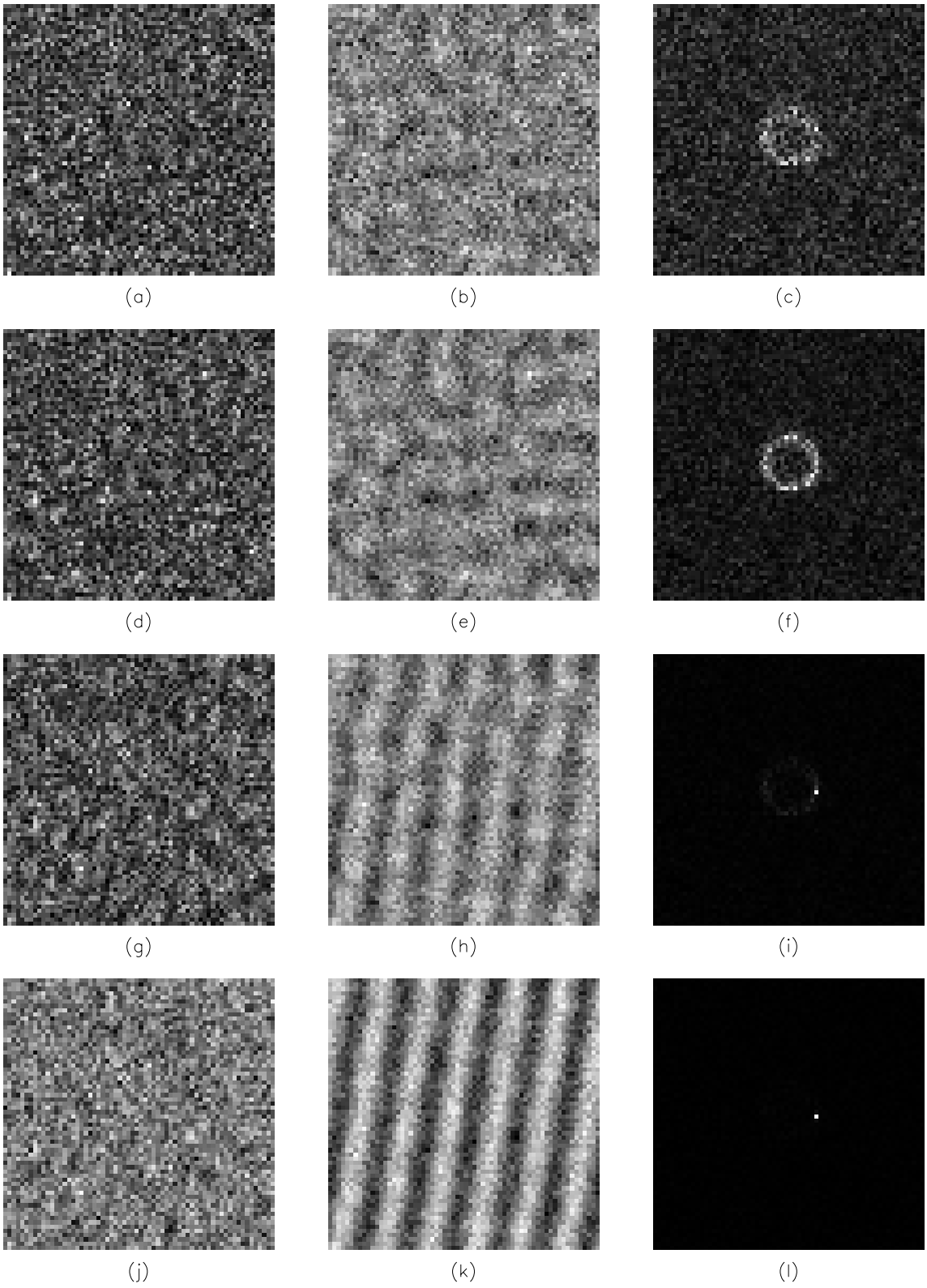

Fig. 9. Snapshots obtained by numerical integration of the nonlinear Langevin equations (9). The left column correspond to the intensity in the near-field, the central one to the real part of the near field, and the right one to the far-field. (a), (b), (c): $\mathcal{A}_0 = 0.97$; (d), (e), (f): $\mathcal{A}_0 = 1.02$; (g), (h), (i): $\mathcal{A}_0 = 1.10$; (j), (k), (l): $\mathcal{A}_0 = 1.15$. The other parameter is $\Delta = -1$.

where M is the 2×2 matrix appearing in (66). By using (69) it is straightforward to show that:

$$\langle\beta_l(\mathbf{k},t)\eta_p^*(\mathbf{k}',t')\rangle = \int_0^t \mathrm{d}t''\left(\mathrm{e}^{M(t-t'')}\right)_{11} \times\sqrt{2\gamma_l}\langle\eta_l(\mathbf{k},t'')\eta_p^*(\mathbf{k}',t')\rangle = \frac{\sqrt{\gamma_l}}{\sqrt{2}}\delta(\mathbf{k}-\mathbf{k}')\theta(t-t')\left(\mathrm{e}^{-M(t-t')}\right)_{11}\delta_{lp} \tag{70a}$$

$$\langle\beta_l(\mathbf{k},t)\eta_p(\mathbf{k}',t')\rangle = \frac{\sqrt{\gamma_p}}{\sqrt{2}}\delta(\mathbf{k}-\mathbf{k}')\theta(t-t')\left(\mathrm{e}^{-M(t-t')}\right)_{12}\delta_{lp} \tag{70b}$$

where $\theta(t-t')$ is the step function that assume the value $1/2$ at $t=t'$.

For equal time ($t=t'$) correlation functions we have:

$$\langle\beta_l(\mathbf{k},t)\eta_p^*(\mathbf{k}',t)\rangle = \frac{\sqrt{\gamma_l}}{2\sqrt{2}}\delta(\mathbf{k}-\mathbf{k}')\delta_{lp} \tag{71}$$

$$\langle\beta_l(\mathbf{k},t)\eta_p(\mathbf{k}',t)\rangle = 0. \tag{72}$$

We are interested in the evolution of the correlation functions $\langle\beta_l(\mathbf{k},t)\beta_l(\mathbf{k}',t)\rangle$ and $\langle\beta_l(\mathbf{k},t)\beta_l^*(-\mathbf{k}',t)\rangle$, as well as the correlation functions between signal and idler $\langle\beta_l(\mathbf{k},t)\beta_p(\mathbf{k}',t)\rangle$ and $\langle\beta_l(\mathbf{k},t)\beta_p^*(-\mathbf{k}',t)\rangle$.

Their equations of motion are readily obtained from equations (66, 70), which gives for $\langle\beta_l(\mathbf{k},t)\beta_l(\mathbf{k}',t)\rangle$, $\langle\beta_l(\mathbf{k},t)\beta_l^*(-\mathbf{k}',t)\rangle$, $\langle\beta_l(\mathbf{k},t)\beta_p(\mathbf{k}',t)\rangle$, $\langle\beta_l(\mathbf{k},t)\beta_p^*(-\mathbf{k}',t)\rangle$:

$$\frac{\partial}{\partial t}\langle\beta_l(\mathbf{k},t)\beta_l(\mathbf{k}',t)\rangle = -\gamma_l[2+\mathrm{i}(\sigma_{lk}+\sigma_{lk'})]\langle\beta_l(\mathbf{k},t)\beta_l(\mathbf{k}',t)\rangle + \sqrt{\gamma_l\gamma_p}\mathcal{A}_0\left(\langle\beta_l(\mathbf{k},t)\beta_p^*(-\mathbf{k}',t)\rangle + \langle\beta_p^*(-\mathbf{k},t)\beta_l(\mathbf{k}',t)\rangle\right),$$

$$\frac{\partial}{\partial t}\langle\beta_l(\mathbf{k},t)\beta_l^*(-\mathbf{k}',t)\rangle = -\gamma_l[2+\mathrm{i}(\sigma_{lk}-\sigma_{lk'})] \times\langle\beta_l(\mathbf{k},t)\beta_l^*(-\mathbf{k}',t)\rangle + \sqrt{\gamma_l\gamma_p}\mathcal{A}_0^*\langle\beta_l(\mathbf{k},t)\beta_p(\mathbf{k}',t)\rangle + \gamma_l\mathcal{A}_0\langle\beta_p^*(-\mathbf{k},t)\beta_l^*(-\mathbf{k}',t)\rangle + \gamma_l\delta(\mathbf{k}+\mathbf{k}'),$$

$$\frac{\partial}{\partial t}\langle\beta_l(\mathbf{k},t)\beta_p(\mathbf{k}',t)\rangle = -[(\gamma_l+\gamma_p)+\mathrm{i}(\gamma_l\sigma_{lk}+\gamma_p\sigma_{pk'})] \times\langle\beta_l(\mathbf{k},t)\beta_p(\mathbf{k}',t)\rangle + \sqrt{\gamma_l\gamma_p}\mathcal{A}_0\left(\langle\beta_l(\mathbf{k},t)\beta_l^*(-\mathbf{k}',t)\rangle + \langle\beta_p^*(-\mathbf{k},t)\beta_p(\mathbf{k}',t)\rangle\right),$$

$$\frac{\partial}{\partial t}\langle\beta_l(\mathbf{k},t)\beta_p^*(-\mathbf{k}',t)\rangle = -[(\gamma_l+\gamma_p)+\mathrm{i}(\gamma_l\sigma_{lk}-\gamma_p\sigma_{pk'})] \times\langle\beta_l(\mathbf{k},t)\beta_p^*(-\mathbf{k}',t)\rangle + \sqrt{\gamma_l\gamma_p}\mathcal{A}_0^*\langle\beta_l(\mathbf{k},t)\beta_l(\mathbf{k}',t)\rangle + \sqrt{\gamma_l\gamma_p}\mathcal{A}_0\langle\beta_p^*(-\mathbf{k},t)\beta_p^*(-\mathbf{k}',t)\rangle. \tag{73}$$

Equations (73) relax after a suitable transient to stationary values. Such values are obtained by solving algebraic equations of the form:

$$B_a\mathbf{V}_a = \mathbf{W}_a, \qquad B_b\mathbf{V}_b = \mathbf{W}_b \tag{74}$$

where the 4×4 B_a and B_b are given by:

see equations (75, 76) below

and where the vectors $\mathbf{V}_a$, $\mathbf{W}_a$, $\mathbf{V}_b$, $\mathbf{W}_b$ are

$$\mathbf{V}_a = \begin{pmatrix}\langle\beta_l(\mathbf{k})\beta_l(\mathbf{k}')\rangle\\ \langle\beta_p^*(-\mathbf{k})\beta_p^*(-\mathbf{k}')\rangle\\ \langle\beta_l(\mathbf{k})\beta_p^*(-\mathbf{k}')\rangle\\ \langle\beta_p^*(-\mathbf{k})\beta_l(\mathbf{k}')\rangle\end{pmatrix}, \quad \mathbf{W}_a = 0, \tag{77}$$

$$\mathbf{V}_b = \begin{pmatrix}\langle\beta_l(\mathbf{k})\beta_p(\mathbf{k}')\rangle\\ \langle\beta_p^*(-\mathbf{k})\beta_l^*(-\mathbf{k}')\rangle\\ \langle\beta_l(\mathbf{k})\beta_l^*(-\mathbf{k}')\rangle\\ \langle\beta_p^*(-\mathbf{k})\beta_p(\mathbf{k}')\rangle\end{pmatrix}, \quad \mathbf{W}_b = \delta(\mathbf{k}+\mathbf{k}')\begin{pmatrix}0\\0\\-\gamma_l\\-\gamma_p\end{pmatrix} \tag{78}$$

The fact that $W_a = 0$ and $\det B_a \neq 0$ implies:

$$\langle\beta_l(\mathbf{k})\beta_l(\mathbf{k}')\rangle = 0. \tag{79}$$

$$B_a = \begin{pmatrix} -\gamma_l[2+\mathrm{i}(\sigma_{lk}+\sigma_{lk'})] & 0 & \sqrt{\gamma_l\gamma_p}\mathcal{A}_0 & \sqrt{\gamma_l\gamma_p}\mathcal{A}_0\\ 0 & -\gamma_p[2-\mathrm{i}(\sigma_{pk}+\sigma_{pk'})] & \sqrt{\gamma_l\gamma_p}\mathcal{A}_0^* & \sqrt{\gamma_l\gamma_p}\mathcal{A}_0^*\\ \sqrt{\gamma_l\gamma_p}\mathcal{A}_0^* & \sqrt{\gamma_l\gamma_p}\mathcal{A}_0 & -[(\gamma_l+\gamma_p)+\mathrm{i}(\gamma_l\sigma_{lk}-\gamma_p\sigma_{pk'})] & 0\\ \sqrt{\gamma_l\gamma_p}\mathcal{A}_0^* & \sqrt{\gamma_l\gamma_p}\mathcal{A}_0 & 0 & -[(\gamma_l+\gamma_p)-\mathrm{i}(\gamma_p\sigma_{pk}-\gamma_l\sigma_{lk'})] \end{pmatrix} \tag{75}$$

$$B_b = \begin{pmatrix} -[(\gamma_l+\gamma_p)+\mathrm{i}(\gamma_l\sigma_{lk}+\gamma_p\sigma_{pk'})] & 0 & \sqrt{\gamma_l\gamma_p}\mathcal{A}_0 & \sqrt{\gamma_l\gamma_p}\mathcal{A}_0\\ 0 & -[(\gamma_l+\gamma_p)-\mathrm{i}(\gamma_p\sigma_{pk}+\gamma_l\sigma_{lk'})] & \sqrt{\gamma_l\gamma_p}\mathcal{A}_0^* & \sqrt{\gamma_l\gamma_p}\mathcal{A}_0^*\\ \sqrt{\gamma_l\gamma_p}\mathcal{A}_0^* & \sqrt{\gamma_l\gamma_p}\mathcal{A}_0 & -\gamma_l[2+\mathrm{i}(\sigma_{lk}-\sigma_{lk'})] & 0\\ \sqrt{\gamma_l\gamma_p}\mathcal{A}_0^* & \sqrt{\gamma_l\gamma_p}\mathcal{A}_0 & 0 & -\gamma_p[2-\mathrm{i}(\sigma_{pk}-\sigma_{pk'})] \end{pmatrix} \tag{76}$$

$$D=\frac{\det B_b}{\gamma_l\gamma_p(\gamma_l+\gamma_p)^2}=\left[1+\mathrm{i}\left(\frac{\gamma_l\sigma_{lk}+\gamma_p\sigma_{pk'}}{\gamma_l+\gamma_p}\right)\right]\left[1-\mathrm{i}\left(\frac{\gamma_p\sigma_{pk}+\gamma_l\sigma_{lk'}}{\gamma_l+\gamma_p}\right)\right][2+\mathrm{i}\,(\sigma_{lk}-\sigma_{lk'})]\,[2-\mathrm{i}(\sigma_{pk}-\sigma_{pk'})]$$
$$-|\mathcal{A}_0|^2\left[2+\mathrm{i}\frac{\gamma_l}{\gamma_l+\gamma_p}(\sigma_{lk}-\sigma_{lk'})-\mathrm{i}\frac{\gamma_p}{\gamma_l+\gamma_p}(\sigma_{pk}-\sigma_{pk'})\right]^2 \quad (80)$$

$$\langle\beta_l(\mathbf{k})\beta_l^*(-\mathbf{k}')\rangle=\left[1+\mathrm{i}\left(\frac{\gamma_l\sigma_{lk}+\gamma_p\sigma_{pk'}}{\gamma_l+\gamma_p}\right)\right]\left[1-\mathrm{i}\left(\frac{\gamma_p\sigma_{pk}+\gamma_l\sigma_{lk'}}{\gamma_l+\gamma_p}\right)\right][2-\mathrm{i}\,(\sigma_{pk}-\sigma_{pk'})]\,\delta(\mathbf{k}+\mathbf{k}')/D$$
$$-|\mathcal{A}_0|^2\frac{\gamma_l-\gamma_p}{\gamma_l+\gamma_p}\left[2+\mathrm{i}\frac{\gamma_l}{\gamma_l+\gamma_p}(\sigma_{lk}-\sigma_{lk'})-\mathrm{i}\frac{\gamma_p}{\gamma_l+\gamma_p}(\sigma_{pk}-\sigma_{pk'})\right]\delta(\mathbf{k}+\mathbf{k}')/D. \quad (81)$$

We define D

see equation (80) above

so that

see equation (81) above

As far as correlation functions between signal and idler are concerned, we have $\langle\beta_l(\mathbf{k})\beta_p^*(-\mathbf{k}')\rangle = 0$ as well as $\langle\beta_p^*(-\mathbf{k})\beta_l(\mathbf{k}')\rangle = 0$,

$$\langle\beta_l(\mathbf{k})\beta_p(\mathbf{k}')\rangle=\frac{\sqrt{\gamma_l\gamma_p}}{\gamma_l+\gamma_p}\left[1-\mathrm{i}\frac{\gamma_p\sigma_{pk}+\gamma_l\sigma_{lk'}}{\gamma_l+\gamma_p}\right]$$
$$\times\,[4+\mathrm{i}(\sigma_{lk}-\sigma_{lk'}-\sigma_{pk}+\sigma_{pk'})]\,\mathcal{A}_0\delta(\mathbf{k}+\mathbf{k}')/D, \quad (82)$$

$$\langle\beta_p^*(-\mathbf{k})\beta_l^*(-\mathbf{k}')\rangle=\frac{\sqrt{\gamma_l\gamma_p}}{\gamma_l+\gamma_p}\left[1+\mathrm{i}\frac{\gamma_l\sigma_{lk}+\gamma_p\sigma_{pk'}}{\gamma_l+\gamma_p}\right]$$
$$\times\,[4+\mathrm{i}(\sigma_{lk}-\sigma_{lk'}-\sigma_{pk}+\sigma_{pk'})]\,\mathcal{A}_0^*\delta(\mathbf{k}+\mathbf{k}')/D. \quad (83)$$

We only need the expression of the correlation function in the particular case where $|\mathbf{k}| = |\mathbf{k}'|$. This happens when k and k' are on the same circle, which is precisely the case when we are looking at the far-field. In this case the correlation functions read:

$$\langle\beta_l(\mathbf{k})\beta_l(\mathbf{k}')\rangle=0, \quad (84)$$

$$\langle\beta_l(\mathbf{k})\beta_l^*(-\mathbf{k}')\rangle=\frac{\left[\left(1+\sigma_k^2\right)-(\gamma_l-\gamma_p)\,(\gamma_l+\gamma_p)^{-1}\,|\mathcal{A}_0|^2\right]\delta(\mathbf{k}+\mathbf{k}')}{2(1+\sigma_k^2-|\mathcal{A}_0|^2)}, \quad (85)$$

where

$$\sigma_k=\Delta+k^2\frac{\gamma_l a_l+\gamma_p a_p}{\gamma_l+\gamma_p}\,. \quad (86)$$

The correlation functions between signal and idler fields are one of the targets of this appendix. We have

$$\langle\beta_l(\mathbf{k})\beta_p^*(-\mathbf{k}')\rangle=0 \quad (87)$$

$$\langle\beta_l(\mathbf{k})\beta_p(\mathbf{k}')\rangle=\left(\frac{\sqrt{\gamma_l\gamma_p}}{\gamma_l+\gamma_p}\right)\left(\frac{[1-\mathrm{i}\sigma_k]\,\mathcal{A}_0\delta(\mathbf{k}+\mathbf{k}')}{1+\sigma_k^2-|\mathcal{A}_0|^2}\right) \quad (88)$$

$$\langle\beta_p^*(\mathbf{k})\beta_l^*(\mathbf{k}')\rangle=\left(\frac{\sqrt{\gamma_l\gamma_p}}{\gamma_l+\gamma_p}\right)\left(\frac{[1+\mathrm{i}\sigma_k]\,\mathcal{A}_0^*\delta(\mathbf{k}+\mathbf{k}')}{1+\sigma_k^2-|\mathcal{A}_0|^2}\right). \quad (89)$$

Appendix B

In the framework of cavity input/output formalism [25], the dynamics of intracavity field operators is described by quantum Langevin differential equations. Below the threshold, where pump depletion can be neglected, the time evolution of signal and idler operators is governed by the following linearised equations:

$$\frac{\partial}{\partial t}A_1(\mathbf{x},t)=-\gamma_1(1+\mathrm{i}\Delta-\mathrm{i}a_1\nabla^2)A_1(\mathbf{x},t)$$
$$+\sqrt{\gamma_1\gamma_2}\mathcal{A}_0A_2^\dagger(\mathbf{x},t)+\sqrt{2\gamma_1}A_1^{\mathrm{in}}(\mathbf{x},t), \quad (90)$$

$$\frac{\partial}{\partial t}A_2(\mathbf{x},t)=-\gamma_2(1+\mathrm{i}\Delta-\mathrm{i}a_2\nabla^2)A_2(\mathbf{x},t)$$
$$+\sqrt{\gamma_1\gamma_2}\mathcal{A}_0A_1^\dagger(\mathbf{x},t)+\sqrt{2\gamma_2}A_2^{\mathrm{in}}(\mathbf{x},t), \quad (91)$$

where A_l^{in}, $(l = 1, 2)$ are noise operators representing input vacuum fluctuations. To these equations we have to add the boundary conditions at the cavity coupling mirror, linking the outgoing fields A_l^{out} to the intracavity fields and the reflected fields:

$$A_l^{\mathrm{out}}(\mathbf{x},t)=\sqrt{2\gamma_l}A_l(\mathbf{x},t)-A_l^{\mathrm{in}}(\mathbf{x},t)\quad(l=1,2). \quad (92)$$

Equations (90, 91) can be easily solved in the temporal and spatial frequency domain. By introducing:

$$A_l(\mathbf{k},\omega)=\int_{-\infty}^{+\infty}\frac{\mathrm{d}t}{\sqrt{2\pi}}\mathrm{e}^{\mathrm{i}\omega t}\int\frac{\mathrm{d}\mathbf{x}}{2\pi}\,\mathrm{e}^{-\mathrm{i}\mathbf{k}\cdot\mathbf{x}}A_l(\mathbf{x},t), \quad (93)$$

and analogous definitions for input and output fields, we obtain:

$$A_1^{\mathrm{out}}(\mathbf{k},\omega)=U_1(\mathbf{k},\omega)A_1^{\mathrm{in}}(\mathbf{k},\omega)+V_1(\mathbf{k},\omega)A_2^{\dagger\,\mathrm{in}}(-\mathbf{k},-\omega),$$
$$A_2^{\mathrm{out}}(\mathbf{k},\omega)=U_2(\mathbf{k},\omega)A_2^{\mathrm{in}}(\mathbf{k},\omega)+V_2(\mathbf{k},\omega)A_1^{\dagger\,\mathrm{in}}(-\mathbf{k},-\omega), \quad (94)$$

with:

$$U_1(\mathbf{k},\omega)=\frac{2\,[1-\mathrm{i}\Delta_2(k,-\omega)]}{[1+\mathrm{i}\Delta_1(k,\omega)]\,[1-\mathrm{i}\Delta_2(k,-\omega)]-|\mathcal{A}_0|^2}-1 \quad (95)$$

$$V_1(\mathbf{k},\omega)=\frac{2\mathcal{A}_0}{[1+\mathrm{i}\Delta_1(k,\omega)]\,[1-\mathrm{i}\Delta_2(k,-\omega)]-|\mathcal{A}_0|^2}, \quad (96)$$

where

$$\Delta_l(\mathbf{k},\omega) = \Delta + a_l k^2 - \frac{\omega}{\gamma_l} \qquad (l=1,2) \tag{97}$$

is the effective detuning parameters for the lth wave, propagating with a transverse wave-vector $\mathbf{k}$ and with a frequency shift ω from the carrier frequency. Functions U_2 and V_2 are obtained from U_1, V_1 by interchanging the indexes 1 and 2 in (95, 96).

By using the fact that the input fields are in vacuum state, second order moments of fields operators are calculated as:

$$F_{ij}(\mathbf{k},\mathbf{k}',\omega) \equiv \int_{-\infty}^{+\infty} \mathrm{d}t\, \mathrm{e}^{-\mathrm{i}\omega t} \langle A_i^{\dagger\,\mathrm{out}}(\mathbf{k},t) A_j^{\mathrm{out}}(\mathbf{k}',0)\rangle \tag{98}$$

$$= \delta_{ij}\delta(\mathbf{k}-\mathbf{k}')\left|V_i(\mathbf{k},\omega)\right|^2, \tag{99}$$

$$D_{ij}(\mathbf{k},\mathbf{k}',\omega) \equiv \int_{-\infty}^{+\infty} \mathrm{d}t\, \mathrm{e}^{-\mathrm{i}\omega t} \langle A_i^{\mathrm{out}}(\mathbf{k},t) A_j^{\mathrm{out}}(\mathbf{k}',0)\rangle \tag{100}$$

$$= (1-\delta_{ij})\delta(\mathbf{k}+\mathbf{k}')U_i(\mathbf{k},\omega)V_j(-\mathbf{k},-\omega). \tag{101}$$

The mean intensity in the Fourier plane is obtained by transforming (99) in time domain:

$$\langle I_i(\mathbf{k})\rangle = \langle A_i^{\dagger\,\mathrm{out}}(\mathbf{k},t) A_i^{\mathrm{out}}(\mathbf{k},t)\rangle$$
$$= \delta(0)\int_{-\infty}^{+\infty} \frac{\mathrm{d}\omega}{2\pi}\left|V_i(\mathbf{k},\omega)\right|^2. \tag{102}$$

Normally ordered moments of field operators of higher order are calculated by factorising in second order moments. For the normally ordered correlation of intensity fluctuations at two different space-time points (in the Fourier plane) we have:

$$G_{ij}(\mathbf{k},\mathbf{k}',\tau=t) = \langle :\, \delta I_i(\mathbf{k},t)\, \delta I_j(\mathbf{k}',0)\, :\rangle \tag{103}$$

$$= \langle A_i^{\dagger\,\mathrm{out}}(\mathbf{k},t) A_j^{\dagger\,\mathrm{out}}(\mathbf{k}',0) A_j^{\mathrm{out}}(\mathbf{k}',0) A_i^{\mathrm{out}}(\mathbf{k},t)\rangle - \langle A_i^{\mathrm{out}}(\mathbf{k},t) A_j^{\mathrm{out}}(\mathbf{k},t)\rangle\langle A_i^{\mathrm{out}}(\mathbf{k}',0) A_j^{\mathrm{out}}(\mathbf{k}',0)\rangle \tag{104}$$

$$= F_{ij}(\mathbf{k},\mathbf{k}',\tau=t)F_{ij}^*(\mathbf{k},\mathbf{k}',\tau=t) + D_{ij}(\mathbf{k},\mathbf{k}',\tau=t)D_{ij}^*(\mathbf{k},\mathbf{k}',\tau=t). \tag{105}$$

Hence the spectrum at frequency ω of the intensity correlation function in the Fourier plane is given by:

$$G_{ij}(\mathbf{k},\mathbf{k}',\omega) = \int_{-\infty}^{+\infty} \mathrm{d}t\, \mathrm{e}^{-\mathrm{i}\omega t} G_{ij}(\mathbf{k},\mathbf{k}',\tau=t) \tag{106}$$

$$= \int_{-\infty}^{+\infty} \frac{\mathrm{d}\omega'}{2\pi} F_{ij}(\mathbf{k},\mathbf{k}',\omega')F_{ij}^*(\mathbf{k},\mathbf{k}',\omega'-\omega) + D_{ij}(\mathbf{k},\mathbf{k}',\omega')D_{ij}^*(\mathbf{k},\mathbf{k}',\omega'-\omega) \tag{107}$$

$$= \delta_{ij}[\delta(\mathbf{k}-\mathbf{k}')]^2 \int \frac{\mathrm{d}\omega'}{2\pi}\left|V_i(\mathbf{k},\omega')\right|^2 \left|V_j(\mathbf{k},\omega'-\omega)\right|^2 + (1-\delta_{ij})[\delta(\mathbf{k}+\mathbf{k}')]^2 \int \frac{\mathrm{d}\omega'}{2\pi} U_i(\mathbf{k},\omega')U_i^*(\mathbf{k},\omega'-\omega) \times V_j(-\mathbf{k},-\omega')V_j^*(-\mathbf{k},-\omega'+\omega). \tag{108}$$

References

1. M.C. Cross, P.C. Hohenberg, Rev. Mod. Phys. **65**, 851 (1993).
2. H. Bénard, Ann. Chim. Phys. **7**, 62 (1900).
3. P. de Kepper, V. Castets, E. Dulos, J. Boissonade, Physica D **49**, 131 (1991).
4. G. Nicolis, *Introduction to Nonlinear Science* (University Press, Cambridge, 1995).
5. J.D. Murray, *Mathematical biology* (Springer, New York, 1989).
6. F.T. Arecchi, Physica D **86**, 297 (1995).
7. *Nonlinear Optical Structures, Patterns and Chaos*, edited by L.A. Lugiato, special issue of Chaos Solitons and Fractal **4**, 1244 (1994).
8. L. Mandel, E. Wolf, *Optical Coherence and Quantum Optics* (Cambridge University Press, Cambridge, 1995).
9. L.A. Lugiato, F. Castelli, Phys. Rev. Lett. **68**, 3284 (1992).
10. L.A. Lugiato, A. Gatti, Phys. Rev. Lett. **70**, 3868 (1993).
11. L.A. Lugiato, I. Marzoli, Phys. Rev. A **52**, 4886 (1995).
12. L.A. Lugiato, G. Grynberg, Europhys. Lett. **29**, 675 (1995).
13. A. Gatti, L.A. Lugiato, Phys. Rev. A **52**, 1675 (1995).
14. A. Gatti, H. Wiedemann, L.A. Lugiato, I. Marzoli, G.-L. Oppo, S. Barnett, Phys. Rev. A **56**, 877 (1997).
15. L.A. Wu, H.J. Kimble, J. Hall, H. Wu, Phys. Rev. Lett. **57**, 2520 (1986).
16. G.-L. Oppo, M. Brambilla, L.A. Lugiato, Phys. Rev. A **49**, 2028 (1994).
17. S. Longhi, Phys. Rev. A **53**, 4488 (1996); J. Mod. Opt. **43**, 1569 (1996).
18. F. Castelli, L.A. Lugiato, J. Mod. Opt. **44**, 765 (1997).
19. A. Gatti, L.A. Lugiato, K.I. Petsas, I. Marzoli, Europhys. Lett. **46**, 461 (1999).
20. G.-L. Oppo, M. Brambilla, D. Camesasca, A. Gatti, L.A. Lugiato, J. Mod. Opt. **41**, 1151 (1994).
21. S. Longhi, J. Mod. Opt. **43**, 1089 (1996).
22. G.-L. Oppo, *EQEC94, Technical Digest*, Amsterdam, 1994; S. Longhi, G.-L. Oppo, W.J. Firth (unpublished).
23. M.L. Berre, D. Leduc, S. Patrascu, E. Ressayre, A. Tallet, Chaos, Solitons and Fractals, **10**, 627 (1999).
24. L.A. Lugiato, A. Gatti, H. Ritsch, I. Marzoli, G.-L. Oppo, J. Mod. Opt. **44**, 1899 (1997).
25. C.W. Gardiner, *Quantum Noise* (Springer-Verlag, Berlin, 1991).
26. For more details see *e.g.* I.V. Sokolov, M.I. Kolobov, L.A. Lugiato, Phys. Rev. A **60**, 2420 (1999).
27. M. Wu, G. Ahlers, D.S. Cannell, Phys. Rev. Lett. **75**, 1743 (1995).
28. A. Gatti, E. Brambilla, L.A. Lugiato, M.I. Kolobov, Phys. Rev. Lett. **83**, 1763 (1999).
29. I. Marzoli, A. Gatti, L.A. Lugiato, Phys. Rev. Lett. **78**, 2092 (1997).
30. C. Fabre, E. Giacobino, A. Heidmann, S. Reynaud, J. Phys. **50**, 1209 (1989).